Eccentricity paced paleoenvironment evolution and microbial community structure in the Gulf of Mexico during the outgoing Early Eocene Climate Optimum

Danlei Wang[1], Lorenz Schwark[1,2], Wolfgang Ruebsam[2], Alex. I. Holman[1], Michael E. Böttcher[3,4,5], Erdem Idiz[6], Marco. J. L. Coolen[1], and Kliti Grice[1*]

[1]*Western Australian Organic and Isotope Geochemistry Centre, School of Earth and Planetary Sciences, Curtin University, Perth, WA 6102, Australia*

[2]*Organic Geochemistry Unit, Institute of Geosciences, Christian-Albrechts-University, Kiel 24118, Germany*

[3]*Geochemistry & Isotope Biogeochemistry Group, Department of Marine Geology, Leibniz Institute for Baltic Sea Research, 18119 Warnemünde, Germany*

[4]*Marine Geochemistry, University of Greifswald, 17489 Greifswald, Germany*

[5]*Department of Maritime Systems, Interdisciplinary Faculty, University of Rostock, 18059 Rostock, Germany*

[6]*Department of Earth Sciences, University of Oxford, Oxford OX1 3AN, UK*

**** Correspondence:*** *K. Grice (k.grice@curtin.edu.au)*

ABSTRACT

Orbital-driven climate fluctuations and associated variations in the carbon cycle over short- and long-term time scales can be recorded in sedimentary archives. Bulk geochemical, biomarker, and stable isotope signatures in sediments deposited at the end of the Early Eocene Climatic Optimum (EECO) recovered from the Chicxulub impact crater in the Gulf of Mexico show a strong relationship with Milankovitch cycles, which play a critical role in controlling climatic and environmental oscillations. Our study represents the first highly spatially-resolved biomarker and bulk geochemical record from the EECO. The bulk $\delta^{13}C_{kerogen}$ data records the Milankovitch eccentricity-paced variability of continental weathering throughout the studied interval. Biomarkers (and indices) indicative of redox conditions [*e.g.,* pristane (Pr)/phytane (Ph) ratios], water column stratification and/or salinity conditions (*e.g.*, Gammacerane Index), photic zone euxinia (*e.g.*, isorenieratane, chlorobactene, and okenane) and those that can differentiate between algal communities such as dinoflagellates (dinosteranes), marine pelagophytes (24-*n*-propylcholestane), chlorophyte algae (24-*iso*-propylcholestane), and prasinophytes (C_{28}/C_{29} sterane ratios) show changes controlled by orbital eccentricity frequencies. In particular, eccentricity maxima were marked by more reducing/salinity stratified water conditions, photic zone euxinic episodes, and higher (relative) abundances of prasinophytes. In contrast, eccentricity minima were marked by more oxic water conditions and an increase in cyanobacterial markers. The $\delta^{13}C$ offset observed between phytane and C_{17} – C_{19} *n*-alkanes may represent shifts between a predominance of autotrophic vs. heterotrophic communities controlled by orbital eccentricity. The direct response of molecular and isotopic composition of organic matter to orbitally controlled climate change in the early Eocene could be proven here for the first time and may be more prevalent in Paleogene sediments worldwide.

1 INTRODUCTION

Earth's orbital parameters change through time in cycles of about 20,000 to 400,000 years (20 to 400 kyr) duration, collectively known as Milankovitch cycles, which include eccentricity (~100 ka and ~405 kyr), obliquity (~41 kyr), and precession (~19 kyr and ~23 kyr) (Milankovitch, 1941; Berger, 1978). Variations in Earth's orbital parameters control the spatial and seasonal differences in amounts of incoming solar radiation (insolation), resulting in climate oscillations and associated variations in the carbon cycle on a broad range of timescales (Lourens and Tuenter, 2009; Boulila et al., 2018). For the entire Cenozoic (Westerhold et al., 2020), especially during the Ypresian stage of the Early Eocene (56 – 47.8 Ma), which includes the Early Eocene Climatic Optimum (EECO), a robust astronomical calibration has been described by Westerhold et al. (2017). Cyclic environmental changes are represented by short (100 kyr) and long (405 kyr) eccentricity, particularly in equatorial regions between 67 and 14 Ma (Westerhold et al., 2020). Strong eccentricity forcing has been documented for the Demerara rise of the equatorial Atlantic (which is closest to the Chicxulub site), the south Atlantic Walvis Ridge (summarized in Westerhold et al., 2017), the Mediterranean Umbria-Marche Basin (Galeotti et al., 2019), the Shatsky rise of the Equatorial Pacific (Westerhold et al., 2018), and the Southwest-Australian Mentelle Basin of the southern Indian Ocean (Vahlenkamp et al., 2020), displaying the global nature of the EECO eccentricity forcing.

Eccentricity-driven seasonality is characterized by sustained dry climates disturbed by short, intense wet periods involving increased continental weathering, rainfall, and storm events leading to major shifts in biome distributions (Ma et al., 2011; Paillard, 2010). Most Eocene eccentricity studies have utilized bulk geochemical parameters (*e.g.*, $\delta^{13}C_{carb}$) and climate-modeling data (Westerhold et al., 2020). Few studies have investigated the molecular-level association of lipid biomarkers in sediments with orbital cyclicity and environmental changes

during the EECO, although the paleoenvironmental and paleoclimatic conditions reconstructed by sedimentary biomarker records have been previously reported (*e.g.*, Crouch et al., 2020). For this study, we conducted biomarker and compound-specific isotope analysis (CSIA, $\delta^{13}C$) of high-resolution samples from core material (Hole M0077A) of the Chicxulub impact crater (Gulf of Mexico) covering the end of the EECO. These data are combined with bulk geochemical investigations ($\delta^{34}S_{pyrite}$, $\delta^{13}C_{kerogen}$, and Rock Eval pyrolysis) to explore the cyclic variability of paleoenvironmental and microbial community structure changes in response to orbital forcing (Yucatán continental shelf, Fig. 1).

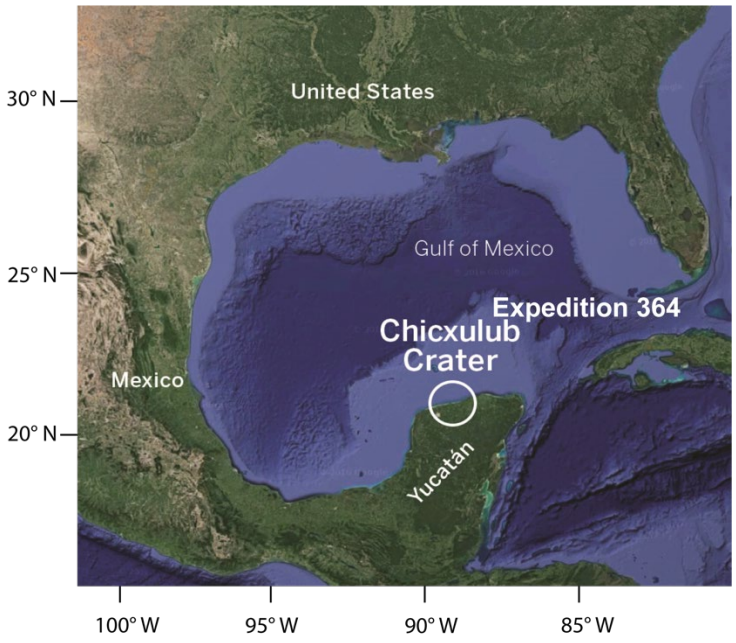

Fig.1. *Location of the drilling site of the Chicxulub impact crater (21.45° N, 89.95° W), Gulf of Mexico, by IODP and ICDP (Expedition 364) in April 2016 (modified from Google Earth, 2021).*

2 MATERIALS AND METHODS

2.1 Sampling and preparation of samples

In April 2016, the Integrated Ocean Discovery Program (IODP) and International Continental Scientific Drilling Program (ICDP) (Expedition 364) recovered a ~800 m-long core (Hole M0077A) in the Chicxulub crater (Gulick et al., 2017). The core was taken from 1334.69 to 505.70 meters below seafloor (mbsf) which captured the Cenozoic interval, including the Cretaceous/Paleogene interval, the Paleocene Eocene Thermal Maximum (PETM), and the EECO. A previous biomarker study was conducted using core samples taken at a relatively lower resolution (62 samples between ~500 to 1300 mbsf) to investigate the post-impact recovery of microbial life and the concomitant paleoenvironmental conditions at the crater site (Schaefer et al., 2020; Schaefer et al., 2022). Here, a total of 69 samples was taken from a ~12 m short interval between ~506.23-518.30 mbsf deposited at the end of the EECO (~48.3 to 48.8Ma) (Gulick et al., 2017; Morgan et al., 2016). Potential contamination on the surface of each intact rock sample was removed in an ultrasonic bath (10 min, three times), using a mixture of organic solvents dichloromethane (DCM) and methanol (MeOH) (9:1). All glassware, including vials, beakers, and pipettes were pre-cleaned and combusted at 500°C (8 hours) to avoid surface contamination.

2. 2 Cyclostratigraphic analysis

Cyclostratigraphic investigations were carried out on color data (L*- and a*-values) obtained from high-resolution line scanning (Gulick et al., 2017). L*- and a*-data were linearly interpolated to an average sampling spacing of 2 cm. After that, data were re-evaluated using the weighted-average rLOESS method. Cyclostratigraphic analysis was initially performed between ~505.72 and 580 mbsf to identify the stable 405 kyr eccentricity cycle (Berger and Loutre, 1994; Laskar et al., 2011; Laskar et al., 2004), followed by a higher resolution analysis of the early Eocene core section ~506 to 522 mbsf used for this study. Cyclostratigraphic analysis was performed using the ACYCLE 2.3 tool for Matlab (Li et al., 2019). For spectral

86 analysis, the 2π multitaper method (MTM) was applied (Thomson, 1982) together with robust
87 red noise models (Mann and Lees, 1996). The frequency ratio method was applied to the data
88 set to test for the presence of astronomical frequencies (Boulila et al., 2008). Evolutionary
89 spectral analysis was done using Fast Fourier transform as implemented in the ACYCLE 2.3
90 tool for Matlab (Li et al., 2019). A sliding window size of 200 and a step size of 2 were used.
91 Evolutionary spectral analysis allows assessing the evolution spectral components along a
92 section investigated. Statistically significant spectral peaks were filtered from the data series
93 using Taner-Hilbert filtering (Taner, 2000).

94 ***2.3 Total organic carbon (TOC) content and Rock-Eval analysis***

95 Total organic carbon (TOC, wt. %) content was measured using a LECO carbon/sulfur analyzer.
96 Rock-Eval pyrolysis was performed on each powered sample (~80 mg) using a Vinci
97 Technologies Rock-Eval 6 standard analyzer with the IFP160000 standard to generate the
98 thermal maturity parameters (S1, S2, Tmax, and S3 peaks). The pyrolysis was programmed at
99 an initial temperature of 300°C (held for 3 min) and then heated to 650°C at a rate of 25°C/min.

100 ***2.4 Carbonate (TIC) content***

101 Total carbon (TC) contents were directly measured on powered samples using a Vario CNS
102 Elemental Analyzer III (Elementar®). Reproducibility and quality of the measurements were
103 checked by running duplicate samples and standards for every tenth sample. The total inorganic
104 carbon (TIC) content in each sample was calculated by subtracting TOC from TC. The
105 carbonate content was calculated by multiplying the TIC by 8.33 (stoichiometry of $CaCO_3$).

106 ***2.5 $\delta^{13}C_{kerogen}$***

107 $\delta^{13}C_{kerogen}$ was measured on decarbonated samples (1M HCl treatment for extracted sediments)
108 using a Thermo Flash 2000 HT elemental analyzer (EA) connected to a Delta V Advantage

isotope ratio mass spectrometer (irMS) via a Conflo IV. Samples were weighed (~2 mg) in triplicate into tin cups (SerCon) and combusted to CO_2 in the nitrogen-carbon reactor (1020 °C). CO_2 passed through the Conflo IV interface into the irMS, which measured *m/z* 44, 45, and 46. $\delta^{13}C$ values were calculated by Thermo Isodat software and normalized to the international VPDB scale by multi-point normalization using the standard reference materials NBS 19 (+1.95 ‰) and L-SVEC (-46.6 ‰) (Coplen et al., 2006). The standard reference material IAEA-600 was measured during the sequence to evaluate the normalization accuracy. The normalized $\delta^{13}C$ values of IAEA-600 from these measurements were within ± 0.1 ‰ of the reported value of -27.8 ‰ (Coplen et al., 2006).

2.6 $^{34}S_{Pyrite}$

The sulfur isotope composition ($\delta^{34}S$) for total reduced inorganic sulfur (TRIS), considered to consist of essentials as pyrite (FeS_2), is represented by $\delta^{34}S_{pyrite}$. The TRIS was extracted from powdered sediments *via* hot acidic chromium (II) chloride distillation. Then the released hydrogen sulfide was transported in a stream of nitrogen gas through a Zn acetate solution trap and precipitated quantitatively as ZnS (Fossing and Jørgensen, 1989). Sulfide concentrations were measured spectrophotometrically using the methylene blue method (Cline, 1969). For isotope measurements, the trapped ZnS was transformed to Ag_2S with a 1 M $AgNO_3$ solution, washed, and dried (*e.g.*, Koebsch et al., 2019). The sulfur isotopic composition was measured by combustion-isotope ratio monitoring mass spectrometry (C-irmMS) using a Thermo Scientific IsoLink elemental analyzer coupled to a Thermo Finnigan MAT 253 mass spectrometer via a Thermo Scientific Conflo IV interface. Mass spectrometric results were calibrated to the V-CDT scale using IAEA isotope reference materials following Mann et al. (2009).

2.7 Biomarker analysis

2.7.1 Soxhlet extraction

The Soxhlet apparatus used for extraction were combusted at 500°C (8 hours) to remove any surface contamination. Before sample extraction, glass-fiber thimbles used for sample extractions were cleaned in the Soxhlet apparatus using 9:1 DCM:MeOH until all traces of organic contaminants were removed. Each ground sample (between 6 ~ 7g) was weighed into the pre-cleaned glass-fiber thimble and was Soxhlet extracted with DCM and MeOH (9:1) (72 hours). At all times, procedural blanks were analyzed in parallel. After extraction, activated copper turnings were added to extracts to remove potential elemental sulfur.

2.7.2 Column chromatography

Sediment extracts (~20 mg) were adsorbed onto activated silica gel and applied on top of a pre-cleaned large column (20 cm) filled with 20 cm of silica gel. The saturated, aromatic, and polar fractions were eluted from the column with the following solvents: *n*-hexane, 9:1 *n*-hexane:DCM, 1:1 DCM:MeOH. All the fractions were reduced to dryness by evaporation under a slow N_2 gas flow.

2.7.3 Gas chromatography – mass spectrometry (GC-MS)

GC-MS was performed using an Agilent 5975B MSD interfaced to an Agilent 6890 gas chromatograph, which was fitted with a DB-1MS UI capillary column for saturated fractions and a DB-5MS UI capillary column for aromatic fractions (both columns J and W Scientific, 60 m, 0.25 mm i.d., 0.25 μm film thickness). Samples were dissolved in *n*-hexane and injected using an Agilent 7683B auto-sampler. The GC oven was ramped from 40 °C to 325 °C at a heating rate of 3 °C/min with initial and final hold times of 1 and 30 min, respectively. Helium was used as carrier gas at a constant flow of 1.1 mL/min. The MS was operated with standardized ionization energy of 70 *eV*, a source temperature of 230 °C, and an electron

multiplier voltage of 1706 V, scanning a mass range of 50–550 Daltons (2.91 scans per second). Saturated and aromatic hydrocarbons were identified by comparison of mass spectra and by matching retention times with those of reference compounds reported previously (Grice et al., 2007; Grice et al., 1996). The mass spectrometer was operated in full scan mode to identify the compounds.

2.7.4 Gas chromatography – metastable reaction mode – mass spectrometry (GC-MRM-MS)

Combined saturated and aromatic fractions with an internal standard added (D4-C_{27} ααα cholestane) were analyzed by GC-QQQ (MRM)-MS at the Massachusetts Institute of Technology (MIT) for quantification, using an Agilent 7890B GC fitted with a DB-5MS UI capillary column (Agilent 122-5562 UI, 60 m, 0.25 mm i. d., 0.25 μm film thickness), connected to an Agilent 7010B triple quadrupole MS. Helium was used as carrier gas. The GC oven was ramped from 40°C to 325°C at a heating rate of 4°C/min with a holding time of 20.75 min at 325 °C. The temperature of the QQQ was set to 150ºC. Compounds were identified by comparing retention time with reference compounds from GEOMARK standards. Specific compounds of interest were identified by comparison with reference standards, matching retention times, and elution order (French et al., 2015). The following transitions were monitored: *m/z* 412 → 191 (C_{30} hopanes), *m/z* 372 → 217 (C_{27} steranes), *m/z* 386 → 217 (C_{28} steranes), *m/z* 400 → 217 (C_{29} steranes), *m/z* 414 → 231 (C_{30} methylsterane), *m/z* 426 → 205 (C_{31} methylhopane), *m/z* 414 → 217 (24-*i*pc), *m/z* 414 → 217 (24-*n*pc), *m/z* 546 → 134 (paleorenieratane & isorenieratane & renieratane & renierapurpurane), *m/z* 552 → 134 (β-paleorenieratane & β-isorenieratane), *m/z* 554 → 134 (chlorobactane & okenane), *m/z* 558 → 123 (β-carotane), *m/z* 560 → 125 (γ-carotane), *m/z* 376.3 → 221 (D4-C_{27} ααα cholestane).

2.7.5 Gas chromatography – isotope ratio – mass spectrometry (GC-*ir*-MS)

Compound-specific $\delta^{13}C$ measurements were performed using a Thermo Trace GC Ultra coupled to a Delta V Advantage irMS *via* a GC Isolink and Conflo IV. GC conditions were the same as described above for saturated compounds. Compounds eluted from the GC were combusted to CO_2 in the GC Isolink combustion furnace (CuO and NiO, held at 1020 °C). Peaks of CO_2 passed through the Conflo interface into the irMS, which measured *m/z* 44, 45, and 46. The $\delta^{13}C$ values were calculated from the measured masses by Thermo Isodat software and normalized to the VPDB scale by comparison with an in-house mixture of *n*-alkanes with known isotopic composition. All samples were analyzed in triplicate.

3 RESULTS AND DISCUSSIONS

3.1 Orbital forcing and age model

3.1.1 Long-term cyclostratigraphic record

Changes in environmental parameters, such as climate, marine primary productivity, or seawater oxygenation at timescales of tens to hundreds of thousands of years can occur in response to orbital forcing, namely Milankovitch cycles (*e.g.*, Hinnov and Hilgen, 2012). Orbitally forced variations in environmental parameters can be expressed by periodic changes in lithological properties [mineral assemblage, carbonate, organic matter, and sulfide (pyrite) contents] of a sediment archive and thereby control the sediment color (*e.g.*, Zhao et al., 2011). The sediment color of core M0077A was determined onboard during expedition 364 (Gulick et al., 2017) and is expressed in the L*a*b* color space. The L-value reflects the lightness, while a*- and b*-values refer to green–red opponent colors and blue–yellow opponents, respectively (International Commission on Illumination).

To identify a cyclicity that occurs in response to the stable 405 kyr long eccentricity (E) cycle (*e.g.*, Hinnov and Hilgen, 2012), cyclostratigraphic analysis was initially performed on an extended core section between 507.72 to 580 mbsf. The preliminary age model based on

biostratigraphic data indicates relatively stable sediment accumulation rates of 2.0-3.5 cm/kyr within this interval (Gulick et al., 2017). Spectral analysis of the detrended L*- and a*-data revealed the presence of various statistically significant spectral peaks (Fig. 2). In both spectrograms (L*- and a*-values), robust spectral peaks occur at frequencies of 0.1 and 0.45 cycles/m. Based on their frequency ratio of about 1:4, spectral peaks were attributed to long (~405 kyr) eccentricity (E) and short (~100 kyr) eccentricity (e) periods. Spectral peaks in the frequency range of 0.8-1.4 cycles/m and 1.6-3.0 cycles/m correspond to the obliquity and precession periods, respectively (Figure 2). The changes in the sediment color indicative of the sediment composition variations occurred in response to orbital forcing. Cyclostratigraphic analysis of the L*- and a*-values further indicate a duration of approx. 2.6 Myr (6.5 x 405 kyr) for foraminiferal zone E7a, which falls in the range of 1.9 to 2.9 Myr calculated by previous studies (Payros et al., 2015; Speijer et al., 2020; Vandenberghe et al., 2012; Westerhold et al., 2017). For the interval between 505.72 and 580 mbsf, we calculated an average sedimentation rate of 2.9 cm/kyr, which agrees with the biostratigraphic age model from Gulick et al. (2017). This close match between our cyclostratigraphic-based duration estimate for zone E7a with previous studies further substantiates the cycle assignment derived here. The interval between 505.72 and 522 mbsf, subject to detailed molecular and isotope geochemical investigations (see sections 3.2 and 3.3), covers almost two long eccentricity cycles and spans about 0.7 Myr (Fig. 2).

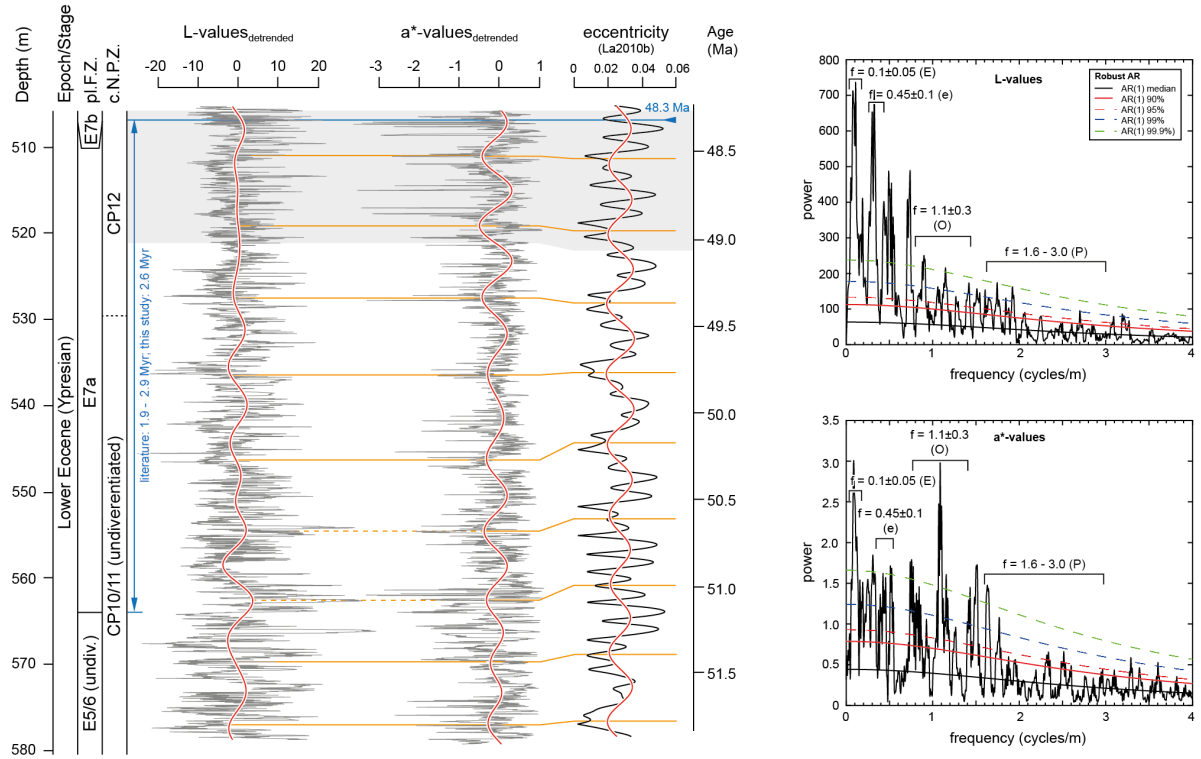

223

224 **Fig. 2.** *Stratigraphic evolution of the detrended (weighted-average rLOESS method; 35%) L*-*
225 *and a*-values (see Gulick et al., 2017) in the depth interval 505.72 to 580 m. Also shown is the*
226 *filter output for the frequency of F = 0.1±0.05 cycles/m, which is attributed to the long*
227 *eccentricity cycle (405 kyr). MTM power spectra for L*- and a*-values are shown in the right*
228 *panel (E: long 405-kyr eccentricity; e: short 100-kyr eccentricity; O: obliquity; P: precession).*
229 *We refer to Gulick et al. (2017) for information on biostratigraphy. Based on the biozone*
230 *boundary dates (Gradstein et al., 2020), a correlation with La2010b solution (Laskar et al.,*
231 *2011) is proposed. See text for discussion. The interval from 505.72 to 522 mbsf (grey shading)*
232 *was subjected to detailed cyclostratigraphic investigations.*

233 **3.1.2 Interval: 505.72 to 522 m**

234 Discrete samples for detailed geochemical investigations were taken from the core from 506.23
235 to 518.63 mbsf. Geochemical parameters determined exhibit a marked periodicity (see sections
236 3.2 and 3.3). To explore the underlying driver(s), we subjected the interval from 505.72 to 522

mbsf to detailed cyclostratigraphic investigations. Sediments are composed of dark mud- and marlstones with serval claystone (presumably volcanic ash beds) and packstone/grainstone (possibly tempestites) interbeds (Fig. 3). In particular, claystone/volcanic ash beds that represent event deposits have the potential to disturb cyclostratigraphic investigations.

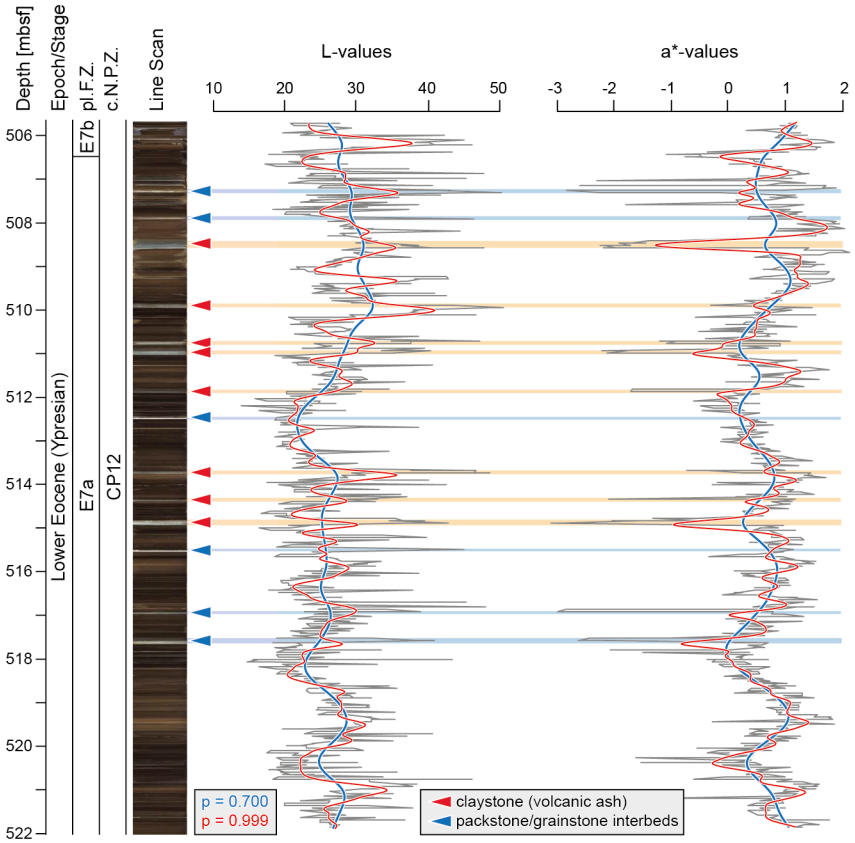

Fig. 3. *Stratigraphic trends in high-resolution L*- and a*-values for the core interval between 506 mbsf and 522 mbsf. Sediments are mainly composed of dark mud- and marlstones, with intercalations of volcanic ash beds and packstone/grainstone horizons. Intercalations, notably volcanic ash beds, represent event deposits that interfere with the accuracy of cyclostratigraphic analysis (Gulick et al., 2017). Red and blue trend lines are smoothing splines with different smooth parameters (p).*

To explore the impact of the event deposits, spectral analysis was carried out for the original data set and the corrected data set after removing the event beds. Power spectra of both the

original and corrected datasets reveal significant spectral peaks at frequencies of about 0.45±0.1 cycles/m that correspond to 2.2 m cycles. This frequency was attributed to the short eccentricity cycle (Fig. 4). Depending on the definition of the filter, 6 to 7 short eccentricity cycles were identified in the interval between 505.72 and 522 mbsf. This results in a duration of about 0.6 to 0.7 Myr, which meets the duration estimate based on the number of long 405 kyr-eccentricity cycles (Figs. 2, 4). Accordingly, removal of the event beds has no significant impact on the spectral peaks in the low-frequency range. However, differences can be observed in the mid-and high-frequency range (f >0.8 cycles/m). In particular, spectral peaks in the frequency range 0.8-1.5 cycles/m that show a high spectral power in the original data partly disappear or show a weaker spectral power in the corrected data set (Fig. 4). In the corrected data, spectral peaks in the frequency range from 1.6 to 3.0 cycles/m are assumed to correspond to the precession cycles (24 kyr, 21 kyr, 17 kyr). Spectral peaks corresponding to obliquity periods might be present as well (0.8-1.4 cycles/m) but show only weak spectral power (Fig. 4). Results are in accordance with data from previous work by Vahlenkamp et al. (2020) and Westerhold et al. (2017, 2018, 2020) that documented a dominant role of eccentricity forcing of environmental evolution during the Early Eocene.

Periodograms of L*- and a*-data indicate minor shifts in the frequency of the short eccentricity cycle, indicating variations in the sediment accumulation rates (Fig. 5). In particular, the interval from about 514-517 mbsf reveals evidence for declined sediment accumulation rates. Variations in sedimentation rates explain minor differences in the filter output in this interval (f=0.4±0.1 versus f=0.45±0.1 cycle/m; see Fig. 5) and thus in the number of short eccentricity cycles that are present in the interval from 505.72-522 m. Assuming a decline in sedimentation rates in the interval from 514-517 mbsf, a duration of 0.7 Myr can be determined for the interval from 505.72-522 mbsf. The resulting sedimentation rate of ~2.3 cm/kyr agrees with a rate of 2.5 cm/kyr previously estimated based on biostratigraphic data in Gulick et al., 2017.

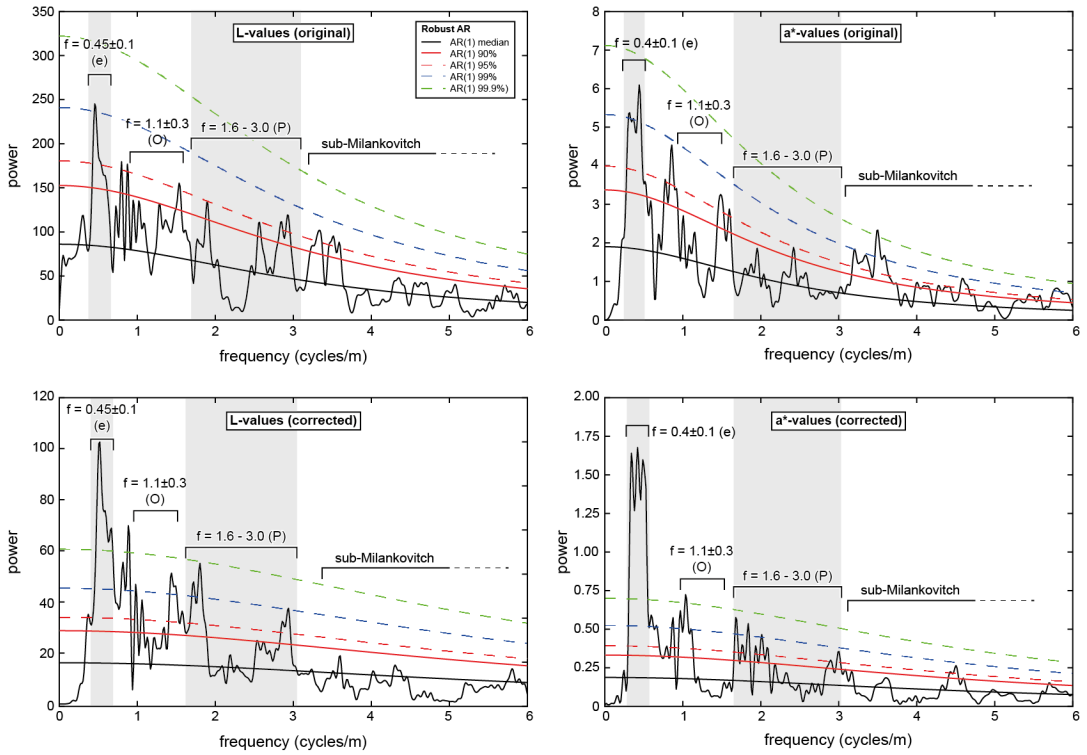

275

276 **Fig. 4.** *MTM power spectra (L* -and a*-values) for the interval sampled. Power spectra are*
277 *shown for the original detrended data (upper panel) and the corrected and detrended data*
278 *(lower panel). In the corrected data set, event layers, such as volcanic ash beds, were removed*
279 *from the data, as they can disturb spectral analysis. In the original and corrected data, spectral*
280 *peaks corresponding to the short eccentricity cycle (e) remain stable. However, in the corrected*
281 *data set, spectral peaks corresponding to the obliquity index (O) and the precession index (P)*
282 *are slightly shifted. This indicates that the removal of the event layer mainly affects high-*
283 *frequency spectral peaks.*

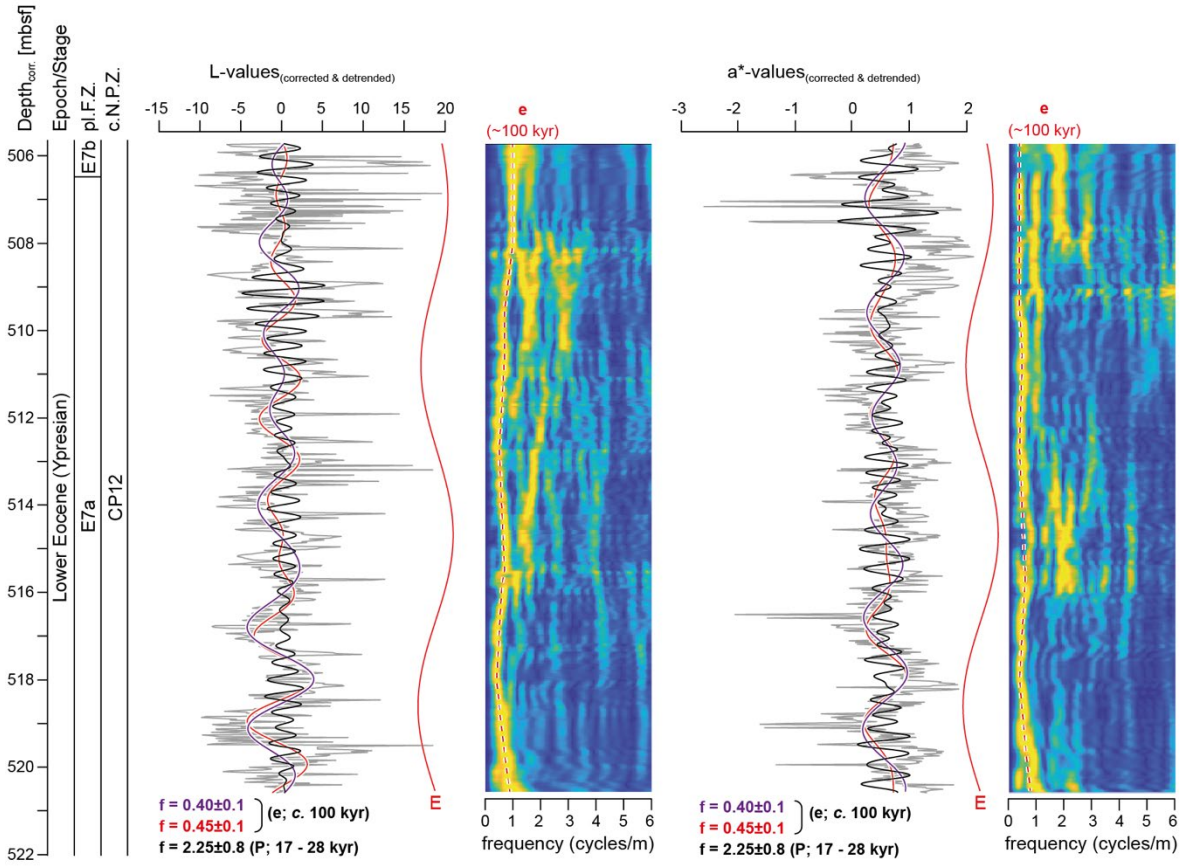

Fig. 5. *Filter output and evolutionary periodograms for corrected L*- and a*-values. Short (~100 kyr) eccentricity (e) and precession (P) cycles have been extracted from the data. Long (~405 kyr) eccentricity cycles (E) are indicated (see Figure 2). Periodograms further show variation in sediment accumulation rates inferred from frequency shifts of the short eccentricity cycle (red dashed line). The interval subjected to detailed molecular investigations (506.23-518.63 mbsf) spans about 0.6 Myr.*

3.2 Bulk Geochemistry

Total organic carbon (TOC) contents, hydrogen index (HI), and oxygen index (OI) values range between 0 – 4 *wt.*%, 71 – 561 (mg HC/g TOC), and 23 – 246 (mg CO_2/g TOC), respectively (Figs. 6 and S1 in the supplementary materials). The higher TOC contents and HIs reflect a greater burial efficiency of organic matter (OM) due to relatively high algal productivity and/or enhanced preservation potential due to reducing depositional environmental conditions (Figs.

297 6 and S1 in the supplementary materials). Lower HI values and higher OI values support a
298 mixture of marine and terrigenous OM deposition (Peters et al., 2005) within the studied
299 interval (Fig. S1 in the supplementary materials). In general, $\delta^{13}C_{kerogen}$ shows cyclical
300 variations paced by the eccentricity frequency (Fig. 6), whereby positive and negative shifts in
301 $\delta^{13}C_{kerogen}$ align to minimal and maximal eccentricity, respectively (Figure 6). If $\delta^{13}C_{kerogen}$
302 composition depends on mixing of isotopically light terrestrial and isotopically heavier marine
303 organic sources, this implies maxima in insolation and eccentricity may have intensified the
304 seasonal dynamics of hydrological cycles and delivered higher proportions of terrigenous OM
305 to the marine depositional environment *via* increased precipitation and run-off. The higher
306 TOC contents at maximum eccentricity can be attributed to enhanced marine productivity due
307 to the supply of nutrients upon enhanced continental run-off, as indicated by elevated HI-values
308 (Fig. S1 in the supplementary materials) derived from marine OM. Enhanced freshwater run-
309 off during maximum eccentricity will have further contributed to freshwater stratification of
310 the water column (Tulipani et al., 2014), leading to oxygen deficiency and elevated OM
311 preservation. In summary, eccentricity-modulated supply and preservation of OM are
312 manifested in the bulk composition of Ypresian sediments at Chicxulub.

313 **3.3 Lipid Biomarkers**

314 In general, lipid biomarker distributions of the sediments show significant fluctuations
315 throughout the core interval *via* saturated compounds, *e.g.,* eukaryotic-derived steroids and
316 bacterial-derived hopanoids, and aromatic compounds, *e.g.,* a range of carotenoids from
317 aerobic and anaerobic photosynthetic bacteria (Fig. 6). Thermal maturity biomarker ratios
318 (Table S1) were consistent with a relatively minor diagenetic alteration of the organic material
319 (Peters et al., 2005). A range of source-diagnostic lipid biomarkers (see below) were evaluated
320 to establish the microbial responses to paleoenvironmental changes linked to orbital forcing.

3.3.1 Biomarkers Indicative of Redox Conditions

Pristane (Pr) and phytane (Ph) are primarily sourced from chlorophyll in phototrophic organisms (Peters et al., 2005). The relative abundances of Pr and Ph (depicted as Pr/Ph) can provide information about palaeo- redox and salinity conditions. Pr/Ph values exhibit cyclical variations (0.54 – 1.18) and generally mirror the eccentricity periodicity (Fig. 6) throughout the studied interval. Relatively low Pr/Ph ratios of ~0.5 to 0.7 are consistent with anoxic conditions and coincide with eccentricity maxima E1 – E6 (Fig. 6), related to higher precipitation and freshwater supply that enhanced water column stratification and anoxia. In contrast, high Pr/Ph ratios of ~0.9 to 1.1 support oxic conditions and coincide with eccentricity minima E1 – E6 (Fig. 6) that represent a drier climate, reduced bioproductivity, and diminished water column stratification.

Gammacerane has been proposed to be a diagenetic product of tetrahymanol, a compound biosynthesised by bacteriovorous ciliates that can thrive at the chemocline of stratified water bodies (Sinninghe Damsté et al., 1995). The relative abundance of gammacerane versus the C_{30} hopane, *i.e.*, the Gammacerane Index (GI), a proxy for water column stratification (Tulipani et al., 2014), fluctuates between 0.02 and 0.12 (Fig. 6). Although higher (lower) GI values seem to occur at eccentricity maxima (minima) (*e.g.*, E6; Fig. 6), the relationships between water stratification and eccentricity cycles remain debated. The GI ratios were generally in low values, and the value range of its fluctuations was small throughout our studied interval. Thus, the GI fluctuations may not necessarily reflect the variability of water stratification conditions. However, given the intensified seasonality during eccentricity maxima (Storm et al., 2020), the restored water-column mixing during dry seasons can average out the gammacerane accumulation caused by high eccentricity wet seasons associated with productivity blooms and bottom-water anoxia. Furthermore, the more stable environmental conditions with constant

accumulation-remineralization balance during eccentricity minima can favor consistent low production of gammaceranes.

Photic zone euxinic (PZE) conditions describe the overlap of the photic zone with the euxinic zone, where in the absence of oxygen, dissolved H_2S is present, the latter formed by the activity of anaerobic sulfate-reducing bacteria (Grice et al., 2005). This may lead to the development of a dense plate of anoxygenic photoautotrophic green and purple sulfur bacteria (GSB and PSB), which use H_2S as an electron donor to fix CO_2 in the presence of sunlight. Biomarkers such as isorenieratane, chlorobactane, and okenane are diagnostic of PZE depositional conditions (*e.g.*, Grice et al., 2005; Schaefer et al., 2020). In the studied interval, isorenieratane (up to 17.7 μg/g TOC), indicative of brown-pigmented GSB, is abundant during eccentricity maxima *e.g.*, E1, E2, E4, E5, and E6 (Fig. 6). Chlorobactane, indicative of green-pigmented GSB, and okenane, indicative of PSB, show fluctuations *albeit* in lower concentrations of <0.2 and <0.3 μg/g TOC, respectively, reaching relatively higher concentrations during eccentricity maxima, in particular, E3 – E6 (Fig. 6). The sulfur bacteria communities are presumed to be predominated by brown-pigmented GSB throughout the studied interval. In addition, variations in the contents (0.09 to 0.99 *dwt.*%) and stable sulfur isotope composition of pyrite ($\delta^{34}S_{pyrite}$, -2.6 to -13.6 ‰) are within the range observed in the aftermath of the Chicxulub impact (Schaefer et al., 2020) and are consistent with episodic PZE conditions (Grice et al., 2005) (Fig. S1, Table S2 in the supplementary materials). The pronounced increase in carbonate and total reduced inorganic sulfur (TRIS) contents with temporary enrichments in $\delta^{34}S_{pyrite,}$ *e.g.*, at ~512.73 mbsf (Fig. S1, Table S2 in the supplementary materials), points to stronger temporal aridity or more closed benthic system sulfate reduction (Hartmann & Nielsen, 2012).

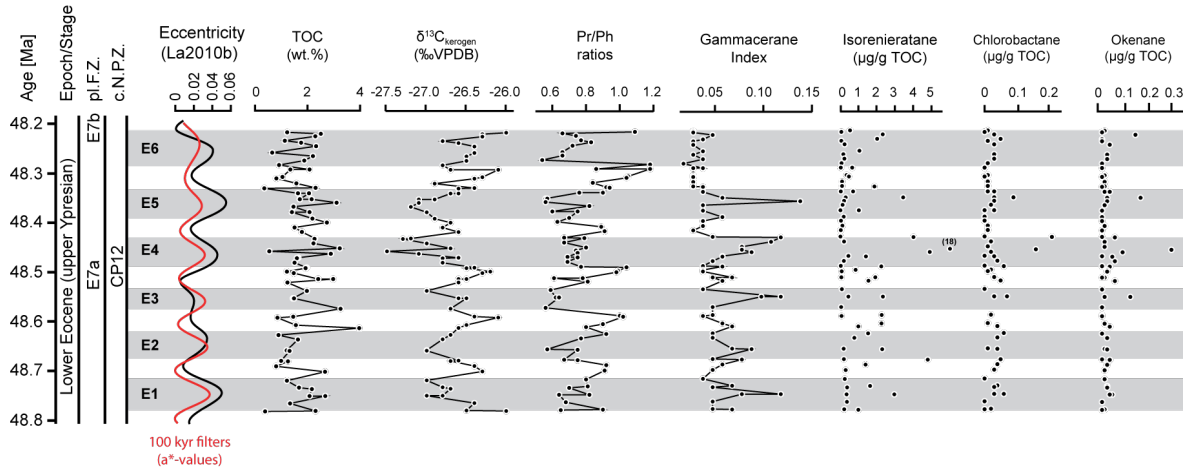

367

368 **Fig. 6.** *Eccentricity frequency calibrated using La2010b (Supplementary Materials), orbital*
369 *solution, corresponding bulk geochemical data (TOC and* $\delta^{13}C_{kerogen}$*), and redox parameters*
370 *of selected biomarkers throughout the studied interval. E1 – E6 represent six short eccentricity*
371 *(e) cycles recorded throughout the interval. Eccentricity maxima (minima) measure how much*
372 *the shape of Earth's orbit departs the most (the least) from a perfect circle. Pr/Ph*
373 *(Pristane/Phytane) – salinity and redox conditions; Gammacerane Index – water stratification;*
374 *isorenieratane – brown pigmented green sulfur bacteria; Chlorobactane – green pigmented*
375 *green sulfur bacteria; Okenane – purple sulfur bacteria. Shaded areas represent intervals*
376 *linked to anoxic conditions.*

377 ***3.3.2 Biomarkers Indicative of Bacterial vs. Eukaryotic Microbial Communities***

378 The hopane/sterane ratio (H/S; Fig. S2 in the supplementary materials) is a commonly used
379 proxy for the relative contributions of bacterial versus eukaryotic biomass (Peters et al., 2005).
380 H/S ranges from 0.10 to 0.61 in the studied interval, supporting an overall predominance of
381 eukaryotic over bacterial contribution to OM in the water column and sedimentary system.
382 Higher H/S values coincide with the E5 and E6 minima (Fig S2 in the supplementary materials),
383 supporting increased contributions of bacteria. However, H/S ratios do not correlate with
384 eccentricity cycles, indicating that enhanced freshwater and nutrient supply did not cause a

385 shift in the primary producer composition. Algal phytoplankton may be differentiated
386 according to its steroid composition (Volkman, 2020). The proportions of C_{27} to C_{29} steranes
387 can reflect changes in phytoplankton populations (Volkman, 2020), whereby the higher ratios
388 of C_{28}/C_{29} steranes (0.67 – 1.26) observed (Fig. 7) may reflect temporal blooms of
389 prasinophytes (Schwark and Empt, 2006). Prasinophytes are resistant to biotic stress (*e.g.*, low
390 oxygen levels) and can be selectively nurtured by the input or availability of nutrients, *e.g.*,
391 reduced nitrogen (Prauss, 2012). In addition to prasinophytes, other phytoplankton groups, *e.g.*,
392 diatoms and coccolithophores, can also produce C_{28} steroids. However, coccolithophores are a
393 particularly dominant group in oligotrophic waters and/or habitats associated with stratified,
394 low nutrient conditions (Litchman, 2007), rendering coccolithophores as potential sources of
395 the C_{28} steranes improbable. In addition, the occurrences of nanofossils assigned to *Coccolithus*
396 *pelagicus* ranged from few to rare throughout most of the studied interval, although the
397 numbers of analyzed specimens were somewhat limited (Guilick et al., 2007). The variations
398 of the biomarker C_{25} highly branched isoprenoid, diagnostic of specific diatom groups
399 (Rowland et al., 2001), show a distinct pattern different from the C_{28}/C_{29} ratios (Figs. 7 and S2
400 in the supplementary materials), indicating diatoms probably did not contribute significantly
401 to the C_{28} steranes in the studied samples either. The presence of 4,23,24–trimethylcholestanes
402 (dinosteranes) indicative of dinoflagellates (Summons and Powell, 1987), C_{30} sterane 24-*n*-
403 propylcholestane (24-*n*pc) indicative of marine pelagophytes (Rohrssen et al., 2015), and C_{30}
404 sterane 24-*iso*-propylcholestane (24-*i*pc) that may derive from chlorophyte algae (Bobrovskiy
405 et al., 2021) suggest a complex algal community structure. However, although an alternative
406 source of 24-*i*pc and 24-*n*pc (Grabenstatter et al., 2013; Love et al., 2020) from sponges cannot
407 be excluded a priori, the threshold values for a spongal origin with relative abundances of more
408 than 0.5 (Love et al., 2020) were not reached arguing against a sponge origin of 24-*i*pc and 24-
409 *n*pc. In the studied interval, the dinosterane (0.57 – 24.81 μg/g TOC), 24-*n*pc (0.21 – 14.06

410 µg/g TOC), and 24-*i*pc (0.04 – 3.44 µg/g TOC) concentrations varied in cycles and appear to
411 be linked to anoxic zones during eccentricity maxima (Fig. 7). The latter are thought to have
412 supported high algal productivity (Fig. 7) *via* elevated nutrient supply *via* freshwater run-off
413 upon maximum insolation. However, degradation in periodic oxic water columns may lead to
414 amplified shifts in biomarker concentrations in our studied interval.

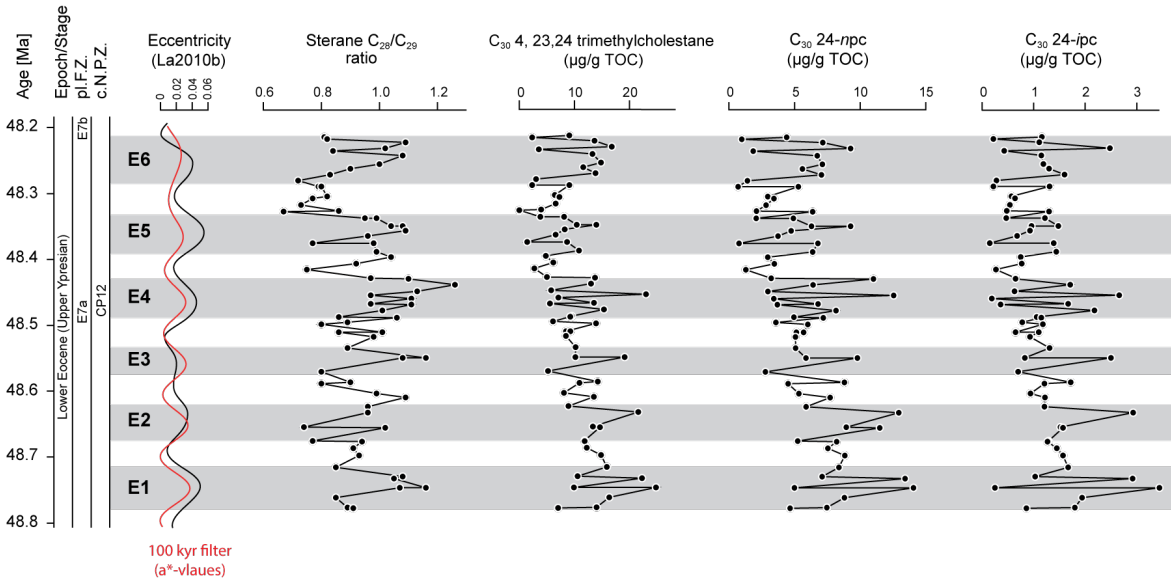

415

416 **Fig. 7.** *Orbital frequency, selected biomarkers indicative of phytoplankton community*
417 *structures throughout the studied interval. An interpretation of each data is indicated below:*
418 *Sterane C_{28}/C_{29} – prasinophytes; C_{30} 4,23,24 trimethylcholestane – dinoflagellates; C_{30} 24-npc*
419 *– marine pelagophytes or sponges; C_{30} 24-ipc – chlorophyte algae or sponges. Shaded areas*
420 *represent intervals linked to anoxic conditions. E1 – E6 represent six short eccentricity cycles*
421 *recorded throughout the short core section.*

422 3β-methyl hopanes are attributed to aerobic proteobacteria, comprising methanotrophs and
423 acetic acid bacteria (Rohmer et al., 1984). Elevated abundances of C_{31} 3β-methyl hopanes
424 relative to C_{30} hopanes (*i.e.*, C_{31} 3-MeH index, up to 0.038) are evident in the E4 maximum
425 (Figure S2), supportive of elevated methanotrophic activity, which may be coupled with

intense methanogenesis as observed in modern euxinic environments, *e.g.*, sulfide-rich sediments and/or in alkaline saline lakes. The relative abundance of C_{31} 2-methylhopane to C_{30} hopanes (*i.e.*, C_{31} 2-MeHI) has been proposed as a proxy for cyanobacterial input to sedimentary OM (Summons et al., 1999). However, there are alternative sources of C_{31} 2-methylhopane, including *α*-proteobacteria from freshwater and terrestrial environments (Ricci et al., 2017). In the studied core section, C_{31} 2-MeHI values (up to 18) are linked to the oxic zones during eccentricity minima E4 and E5 (Fig. S2 in the supplementary materials), suggesting a source of 2-methylhopanes from cyanobacteria. Based on these results, eccentricity cycles did not play a dominant role in controlling the methanotrophic and cyanobacterial activities throughout the studied interval.

The $\delta^{13}C$ of Ph (of selected samples) is shown in Table S3. Ph is predominantly derived from the phytyl side chain of chlorophyll *a* found in phytoplankton and higher land plants. However, methanogenic and halophilic archaea could also be sources of Ph (Peters et al., 2005). In the current interval, periodic positive shifts in $\delta^{13}C_{phytane}$ (-33.8 ‰ ~ -29.1 ‰) linked to anoxic and stratified water conditions may be explained by increased phytoplankton productivity (Fig. 8), assuming that there was no significant change in the $\delta^{13}C$ of dissolved inorganic carbon utilized by phytoplankton during deposition. C_{17}–C_{18} *n*-alkanes can be derived from multiple sources, including primary producers (*e.g.*, algae and cyanobacteria) and heterotrophs (*e.g.*, bacteria). Primary sourced C_{17}–C_{18} *n*-alkanes are depleted in ^{13}C by up to 1.5 ‰ relative to *e.g.*, phytol, while an enrichment of ^{13}C in *n*-alkanes can result from heterotrophic reworking (Grice et al., 2005). The difference between averaged $\delta^{13}C$ values of C_{17}–C_{18} *n*-alkanes and Ph (Fig. 8) in the samples suggests periodic shifts between primary producers (*e.g.*, algae and cyanobacteria), which inhabited the oxygenated photic zone during stratified and anoxic conditions, and heterotrophic communities (*e.g.*, heterotrophic bacteria), which dominated during periods of complete water column mixing (Fig. 8). Our molecular isotope data supported that the

451 eccentricity cyclicity played a key role in controlling the variability of microbial community
452 structures (autotrophs versus heterotrophs) during the end of the EECO at the studied site.

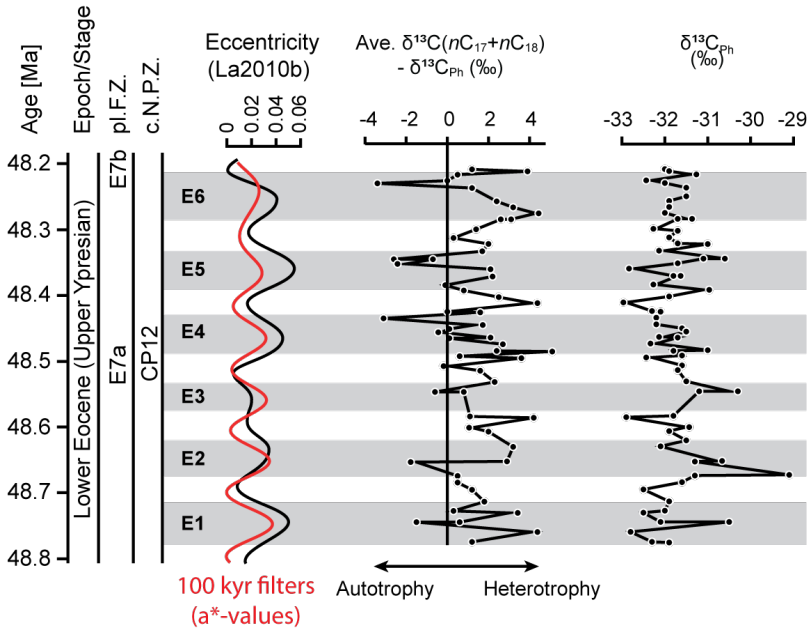

453

454 **Fig. 8.** *Eccentricity frequency and compound-specific carbon isotope data of select biomarkers*
455 *throughout the studied interval. Ave.* $\delta^{13}C$ *(n-*C_{17} *+ n-*C_{18}*) –* $\delta^{13}C$ *of phytane = the difference*
456 *between averaged* $\delta^{13}C$ *values of* C_{17} *–* C_{18} *n-alkanes and* $\delta^{13}C$ *values of phytane;* $\delta^{13}C_{Ph}$ =
457 $\delta^{13}C$ *values of phytane. Shaded areas represent intervals linked to anoxic conditions.*

458 **4 CONCLUSIONS**

459 This is the first high-resolution geochemical biomarker and stable isotope study documenting
460 orbital-paced variability of paleoenvironments and microbial community structure at the end
461 of the EECO. Molecular indices such as Pr/Ph, GI, PZE markers, and prasinophyte C_{28} steranes
462 concur with bulk geochemical parameters (*i.e.*, bulk $\delta^{13}C_{kerogen}$, Rock-Eval data) reflect cyclical
463 variations with eccentricity maxima and minima. Differences in $\delta^{13}C$ between Ph and C_{17}-C_{18}
464 *n*-alkanes reflect eccentricity-controlled periodic shifts between autotrophy and heterotrophy.
465 Environmental conditions at the Chicxulub site during the Ypresian were controlled by high

eccentricity and insolation driving an accelerated hydrological cycle. During maxima in eccentricity, increased precipitation and concomitant nutrient and freshwater run-off led to high marine productivity and more intense water column stratification.

5 ACKNOWLEDGMENTS

This study was supported by Australian Research Council Discovery (DP180100982, Grice, Coolen, and Summons), the International Ocean Discovery Program (IODP), and Australian and New Zealand legacy IODP funding (364 post-cruise funding, 2016–2018) of 'The Chicxulub post-impact crater record'. D.W. was supported by an Australian-Chinese doctoral scholarship from the Chinese Scholarship Council and Curtin University. L.S. acknowledges funding by German Research Foundation grant Schw554/29-1. We thank the scientific party of the IODP Expedition 364 for support on board the LB Myrtle, Roger Everett Summons, and Xingqian Cui at the Summons' Lab for analytical support.

6 REFERENCES CITED

Berger, A., 1978. Long-term variations of daily insolation and Quaternary climatic changes, J. Atmos. Sci., 35, 2362–2367.

Berger, A., Loutre, M.F., 1994. Precession, Eccentricity, Obliquity, Insolation and Paleoclimates, in Duplessy, J.C., Spyridakis, M.T. (Eds), Long-Term Climatic Variations. NATO ASI Series, 22. Springer, Berlin, Heidelberg. https://doi.org/10.1007/978-3-642-79066-9_5.

Bobrovskiy, I., Hope, J.M., Nettersheim, B.J., Volkman, J.K., Hallmann, C., Brocks, J.J., 2021. Algal origin of sponge sterane biomarkers negates the oldest evidence for animals in the rock record. Nat. Ecol. Evol. 5, 165-168. https://doi.org/10.1038/s41559-020-01334-7.

Boulila, S., Hinnov, L.A., Huret, E., Collin, P.-Y., Galbrun, B., Fortwengler, D., Marchand, D., Thierry, J., 2008. Astronomical calibration of the Early Oxfordian (Vocontian and Paris basins, France): Consequences of revising the Late Jurassic time scale. Earth Planet. Sci. Lett. 276, 40-51. https://doi.org/10.1016/j.epsl.2008.09.006.

Boulila, S., Laskar, J., Haq, B.U., Galbrun, B., Hara, N., 2018. Long-term cyclicities in Phanerozoic sea-level sedimentary record and their potential drivers. Glob. Planet. Change 165, 128-136. https://doi.org/10.1016/j.gloplacha.2018.03.004.

Cline, J.D., 1969. SPECTROPHOTOMETRIC DETERMINATION OF HYDROGEN SULFIDE IN NATURAL WATERS1. Limnol. Oceanogr. 14, 454-458. https://doi.org/10.4319/lo.1969.14.3.0454.

Coplen, T.B., Brand, W.A., Gehre, M., Gröning, M., Meijer, H.A.J., Toman, B., Verkouteren, R. M., 2006. New Guidelines for $\delta^{13}C$ Measurements. Anal. Chem. 78, 2439-2441. https://doi.org/10.1021/ac052027c.

Crouch, E.M., Shepherd, C.L., Morgans, H.E.G., Naafs, B.D.A., Dallanave, E., Phillips, A., Hollis, C.J., Pancost, R.D., 2020. Climatic and environmental changes across the early Eocene climatic optimum at mid-Waipara River, Canterbury Basin, New Zealand. Ear. Sci. Rev. 200, 102961. https://doi.org/10.1016/j.earscirev.2019.102961

Fossing, H., Jørgensen, B.B., 1989. Measurement of bacterial sulfate reduction in sediments: evaluation of a single-step chromium reduction method. Biogeochemistry 8, 205–222. https://doi.org/10.1007/BF00002889.

French, K.L., Hallmann, C., Hope, J.M., Schoon, P.L., Zumberge, J.A., Hoshino, Y., Peters, C.A., George, S.C., Love, G.D., Brocks, J.J., Buick, R., Summons, R.E., 2015. Reappraisal of

510 hydrocarbon biomarkers in Archean rocks. Proc. Natl. Acad. Sci. 112, 5915-5920.
511 https://doi.org/10.1073/pnas.1419563112.

512 Galeotti, S., Sprovieri, M., Rio, D., Moretti, M., Francescone, F., Sabatino, N., Fornaciari, E.,
513 Giusberti, L., Lanci, L., 2019. Stratigraphy of early to middle Eocene hyperthermals from
514 Possagno (Southern Alps, Italy) and comparison with global carbon isotope records.
515 Palaeogeogr. Palaeoclimatol. Palaeoecol. 527, 39-52.
516 https://doi.org/10.1016/j.palaeo.2019.04.027.

517 Grabenstatter, J., Méhay, S., McIntyre-Wressnig, A., Giner, J.-L., Edgcomb, V.P., Beaudoin,
518 D.J., Bernhard, J.M., Summons, R.E., 2013. Identification of 24-n-propylidenecholesterol in a
519 member of the Foraminifera. Org. Geochem. 63, 145-151.
520 https://doi.org/10.1016/j.orggeochem.2013.08.010.

521 Gradstein, F.M., Ogg, J.G., Schmitz, M.D., Ogg, G.M., 2020. Geological Timescale 2020,
522 Volume 2. Elsevier, Boston. https://doi.org/10.1016/B978-0-12-824360-2.00047-4.

523 Grice, K., Cao, C., Love, G.D., Böttcher, M.E., Twitchett, R.J., Grosjean, E., Summons, R.E.,
524 Turgeon, S.C., Dunning, W., Jin, Y., 2005. Photic Zone Euxinia During the Permian-Triassic
525 Superanoxic Event. Science 307, 706-709. https://doi.org/10.1126/science.1104323.

526 Grice, K., Nabbefeld, B., Maslen, E., 2007. Source and significance of selected polycyclic
527 aromatic hydrocarbons in sediments (Hovea-3 well, Perth Basin, Western Australia) spanning
528 the Permian–Triassic boundary. Org. Geochem. 38, 1795-1803.
529 https://doi.org/10.1016/j.orggeochem.2007.07.001.

530 Grice, K., Schaeffer, P., Schwark, L., and Maxwell, J. R., 1996. Molecular indicators of
531 palaeoenvironmental conditions in an immature Permian shale (Kupferschiefer, Lower Rhine

532 Basin, north-west Germany) from free and S-bound lipids. Org. Geochem. 25, 131-147.
533 https://doi.org/10.1016/S0146-6380(96)00130-1.

534 Gulick, S.P.S., Morgan, J.V., Mellett, C.L., Green, S.L., Bralower, T., Chenot, E., Christeson,
535 G., Claeys, P., Cockell, C., Coolen, M.J.L., Ferrière, L., Gebhardt, C., Goto, K., Jones, H.,
536 Kring, D., Lofi, J., Lowery, C., Ocampo-Torres, R., Perez-Cruz, L., Pickersgill, A.E., 2017.
537 Chicxulub: Drilling the K-Pg Impact Crater. Proceedings of the International Ocean Discovery
538 Program, 364: College Station, TX (International Ocean Discovery Program).
539 https://doi.org/10.14379/iodp.proc.364.2017.

540 Hartmann, M., Nielsen, H., 2012. $\delta^{34}S$ values in recent sea sediments and their significance
541 using several sediment profiles from the western Baltic Sea. Isoto. Environ. Health Stud. 48,
542 7–32. https://doi.org/10.1080/10256016.2012.660528.

543 Hinnov, L. A., Hilgen, F.J., 2012. Chapter 4 - Cyclostratigraphy and Astrochronology, in
544 Gradstein, F.M., Ogg, J.G., Schmitz, M.D., Ogg, G.M. (Eds.), The Geologic Time Scale.
545 Elsevier, Boston, pp.63-83.

546 Koebsch, F., Winkel, M., Liebner, S., Liu, B., Westphal, J., Schmiedinger, I., Spitzy, A., Gehre,
547 M., Jurasinski, G., Köhler, S., Unger, V.R., Koch, M., Sachs, T., Böttcher, M.E., 2019. Sulfate
548 deprivation triggers high methane production in a disturbed and rewetted coastal peatland.
549 Biogeosciences, 16, 1937-1953. https://doi.org/10.5194/bg-16-1937-2019.

550 Laskar, J., Fienga, A., Gastineau, M., Manche, H., 2011. La2010: a new orbital solution for the
551 long-term motion of the Earth. Astron. Astrophys. 532, A89. https://doi.org/10.1051/0004-
552 6361/201116836, 2011a.

553 Laskar, J., Robutel, P., Joutel, F., Gastineau, M., Correia, A.C.M., Levrard, B., 2004. A long-
554 term numerical solution for the insolation quantities of the Earth. Astron. Astrophys. 428, 261-
555 285. https://doi.org/10.1051/0004-6361:20041335.

556 Li, M., Hinnov, L., Kump, L., 2019. Acycle: Time-series analysis software for paleoclimate
557 research and education. Comput. Geosci. 127, 12-22.
558 https://doi.org/10.1016/j.cageo.2019.02.011.

559 Litchman, E., 2007. Chapter 16 – Resource Competition and the Ecological Success of
560 Phytoplankton, in Falkowski, P.G., Knoll, A.H., (Eds.), Evolution of Primary Producers in the
561 Sea. Academic Press, pp.351-375. https://doi.org/10.1016/B978-012370518-1/50017-5.

562 Lourens, L.J., Tuenter, E., 2009. Chpater 5 - The Role of Variations of the Earth's Orbital
563 Characteristics in Climate Change, in Trevor M.L. (Eds), Climate Change, Elsevier, pp.103-
564 123. https://doi.org/10.1016/B978-0-444-53301-2.00005-1.

565 Love, G.D., , J.A., Cárdenas, P., Sperling, E.A., Rohrssen, M., Grosjean, E., Grotzinger, J.P.,
566 Summons, R.E., 2020. Sources of C_{30} steroid biomarkers in Neoproterozoic–Cambrian rocks
567 and oils. Nat. Ecol. Evol. 4, 34-36. https://doi.org/10.1038/s41559-019-1048-2.

568 Ma, W., Tian, J., Li, Q., Wang, P., 2011. Simulation of long eccentricity (400-kyr) cycle in
569 ocean carbon reservoir during Miocene Climate Optimum. Weathering and nutrient response
570 to orbital change. Geophys. Res. Lett. 38, https://doi.org/10.1029/2011GL047680.

571 Mann, J., Vocke, R., Kelly, W., 2009. Revised δ 34 S reference values for IAEA sulfur isotope
572 reference materials S-2 and S-3. Rapid Commun. Mass Spectrom. 23, 1116-1124.
573 https://doi.org/10.1002/rcm.3977.

574 Mann, M.E., Lees, J.M., 1996. Robust estimation of background noise and signal detection in
575 climatic time series. Clim. Change 33, 409-445. https://doi.org/10.1007/BF00142586.

576 Milankovitch, M., 1941. Kanon der Erdbestrahlung und seine Anwendung auf das
577 Eiszeitenproblem. Royal Serbian Academy, Section of Mathematical and Natural Sciences,
578 33, Belgrade.

579 Morgan, J.V., Gulick, S.P.S., Bralower, T., Chenot, E., Christeson, G., Claeys, P., Cockell, C.,
580 Collins, G.S., Coolen, M.J.L., Ferrière, L., Gebhardt, C., Goto, K., Jones, H., Kring, D.A., Le
581 Ber, E., Lofi, J., Long, X., Lowery, C., Mellett, C., Ocampo-Torres, R., Osinski, G. R., Perez-
582 Cruz, L., Pickersgill, A., Poelchau, M., Rae, A., Rasmussen, C., Rebolledo-Vieyra, M., Riller,
583 U., Sato, H., Schmitt, D. R., Smit, J., Tikoo, S., Tomioka, N., Urrutia-Fucugauchi, J., Whalen,
584 M., Wittmann, A., Yamaguchi, K.E., Zylberman, W., 2016. The formation of peak rings in
585 large impact craters. Science, 354, 878-882. https://doi.org/10.1126/science.aah6561.

586 Oehlert, A.M., Swart, P.K., 2014. Interpreting carbonate and organic carbon isotope covariance
587 in the sedimentary record. Nat. Commun. 5, 4672. https://doi.org/10.1038/ncomms5672

588 Paillard, D., 2010. Climate and the orbital parameters of the Earth. C. R. - Geosci. 342, 273-
589 285. https://doi.org/10.1016/j.crte.2009.12.006.

590 Payros, A., Ortiz, S., Millán, I., Arostegi, J., Orue-Etxebarria, X., Apellaniz, E., 2015. Early
591 Eocene climatic optimum: Environmental impact on the North Iberian continental margin.
592 Geol. Soc. Am. Bull. 127, 1632-1644. https://doi.org/10.1130/B31278.1.

593 Peters, K.E., Walters, C.C., Moldowan, J.M., 2005. The Biomarker Guide, The Biomarker
594 Guide: Biomarkers and Isotopes in Petroleum Systems and Earth History. Cambridge
595 University Press, Cambridge.

596 Prauss, M.L., 2012. The Cenomanian/Turonian Boundary Event (CTBE) at Tarfaya, Morocco,
597 northwest Africa: Eccentricity controlled water column stratification as major factor for total
598 organic carbon (TOC) accumulation: Evidence from marine palynology. Cretaceous Research,
599 37, 246-260. https://doi.org/10.1016/j.cretres.2012.04.007.

600 Ricci, J.N., Morton, R., Kulkarni, G., Summers, M.L., Newman, D.K., 2017. Hopanoids play
601 a role in stress tolerance and nutrient storage in the cyanobacterium *Nostoc punctiforme*.
602 Geobiology 15, 173-183. https://doi.org/10.1111/gbi.12204.

603 Rohmer, M., Bouvier-Nave, P., Ourisson, G., 1984. Distribution of Hopanoid Triterpenes in
604 Prokaryotes. Microbiology 130, 1137-1150. https://doi.org/10.1099/00221287-130-5-1137.

605 Rohrssen, M., Gill, B.C., Love, G.D., 2015. Scarcity of the C30 sterane biomarker, 24-n-
606 propylcholestane, in Lower Paleozoic marine paleoenvironments. Org. Geochem. 80, 1-7.
607 https://doi.org/10.1016/j.orggeochem.2014.11.008.

608 Rowland, S.J., Belt, S.T., Wraige, E.J., Massé, G., Roussakis, C., Robert, J.M., 2001. Effects
609 of temperature on polyunsaturation in cytostatic lipids of *Haslea ostrearia*. Phytochemistry,
610 56, 597-602. https://doi.org/10.1016/S0031-9422(00)00434-9.

611 Schaefer, B., Grice, K., Coolen, M.J.L., Summons, R.E., Cui, X., Bauersachs, T., Schwark, L.,
612 Böttcher, M.E., Bralower, T.J., Lyons, S.L., Freeman, K.H., Cockell, C.S., Gulick, S.P.S.,
613 Morgan, J.V., Whalen, M.T., Lowery, C.M., Vajda, V., 2020. Microbial life in the nascent
614 Chicxulub crater. Geology 48, 328-332. https://doi.org/10.1130/G46799.1.

615 Schaefer, B., Schwark, L., Böttcher, M. E., Smith, V., Coolen, M. J. L., and Grice, K., 2021,
616 Paleoenvironmental evolution during the Early Eocene Climatic Optimum in the Chicxulub
617 impact crater. Earth and Planetary Science Letters, 589, 117589.
618 https://doi.org/10.1016/j.epsl.2022.117589.

619 Schwark, L., Empt, P., 2006. Sterane biomarkers as indicators of palaeozoic algal evolution
620 and extinction events. Palaeogeogr. Palaeoclimatol. Palaeoecol. 240, 225-236.
621 https://doi.org/10.1016/j.palaeo.2006.03.050.

622 Sinninghe Damsté, J.S., Kenig, F., Koopmans, M.P., Köster, J., Schouten, S., Hayes, J.M., de
623 Leeuw, J.W., 1995. Evidence for gammacerane as an indicator of water column stratification.
624 Geochim. Cosmochim. Acta 59, 1895-1900. https://doi.org/10.1016/0016-7037(95)00073-9.

625 Speijer, R.P., Pälike, H., Hollis, C.J., Hooker, J.J., Ogg, J.G., 2020. Chapter 28 - The Paleogene
626 Period, in Gradstein, F.M., Ogg, J.G., Schmitz, M.D., Ogg, G.M., (Eds.), Geologic Time Scale
627 2020. Elsevier, Boston, pp.1087-1140.

628 Storm, M.S., Hesselbo, S.P., Jenkyns, H.C., Gorbanenko O., 2020. Orbital pacing and secular
629 evolution of the Early Jurassic carbon cycle. Proc. Natl. Acad. Sci. U. S. A. 117, 3974-3982.
630 https://doi.org/10.1073/pnas.1912094117.

631 Summons, R.E., Powell, T.G., 1987. Identification of aryl isoprenoids in source rocks and
632 crude oils: Biological markers for the green sulfur bacteria. Geochim. Cosmochim. Acta 51,
633 557-566. https://doi.org/10.1016/0016-7037(87)90069-X.

634 Summons, R.E., Jahnke, L.L., Hope, J.M., Logan, G.A., 1999. 2-Methylhopanoids as
635 biomarkers for cyanobacterial oxygenic photosynthesis. Nature 400, 554-557.
636 https://doi.org/10.1038/23005.

637 Taner, M.T., 2000. Attributes Revisited, Technical Report. Rock Solid Images, Inc.
638 http://www.rocksolidimages.com/pdf/attrib_revisited.htm.

639 Thomson, D. J., 1982. Spectrum estimation and harmonic analysis. Proc. IEEE Inst. Electr.
640 Electron Eng. 70, 1055-1096. https://doi.org/10.1109/PROC.1982.12433.

641 Tulipani, S., Grice, K., Greenwood, P., Haines, P., Sauer, P., Schimmelmann, A., Summons,
642 R., Foster, C., Böttcher, M.E., Playton, T., Schwark, L., 2014. Changes of palaeoenvironmental
643 conditions recorded in Late Devonian reef systems from the Canning Basin, Western Australia:
644 A biomarker and stable isotope approach. Gondwana Res. 28, 1500-1515.
645 https://doi.org/10.1016/j.gr.2014.10.003.

646 Vandenberghe, N., Hilgen, F.J., Speijer, R.P., Ogg, J.G., Gradstein, F.M., Hammer, O., Hollis,
647 C.J., Hooker, J.J., 2012. Chapter 28 - The Paleogene Period, in Gradstein, F.M., Ogg, J.G.,
648 Schmitz, M.D., Ogg, G.M., (Eds.), The Geologic Time Scale. Elsevier, Boston, pp.855-921.

649 Vahlenkamp, M., De Vleeschouwer, D., Batenburg, S.J., Edgar, K.M., Hanson, C.E., Martinez,
650 M., Pälike, H., MacLeod, K.G., Li, Y.-X., Richter, C., Bogus, K.A., Hobbs, R.W., Huber, B.T.,
651 Expedition 369 Scientific Party, 2020. Lower to middle Eocene astronomically-tuned Ca/Fe-
652 ratios and bulk stable isotopes of IODP Site 369-U1514, PANGAEA.
653 https://doi.org/10.1594/PANGAEA.912004.

654 Volkman, J.K., 2020. Lipids of Geochemical Interest in Microalgae, in Wilkes, H., (Ed.),
655 Hydrocarbons, Oils and Lipids: Diversity, Origin, Chemistry and Fate. Handbook of
656 Hydrocarbon and Lipid Microbiology. Springer, Cham, pp.159-191.
657 https://doi.org/10.1007/978-3-319-90569-3_10.

658 Westerhold, T., Marwan, N., Drury, A.J., Liebrand, D., Agnini, C., Anagnostou, E., Barnet, J.
659 S.K., Bohaty, S.M., Vleeschouwer, D.D., Florindo, F., Frederichs, T., Hodell, D.A., Holbourn,
660 A.E., Kroon, D., Lauretano, V., Littler, K., Lourens, L.J., Lyle, M., Pälike, H., Röhl, U., Tian,
661 J., Wilkens, R.H., Wilsons, P.A., Zachos, J.C., 2020. An astronomically dated record of Earth's
662 climate and its predictability over the last 66 million years. Science 369, 1383-1387.
663 https://doi.org/10.1126/science.aba6853.

664 Westerhold, T., Röhl, U., Frederichs, T., Agnini, C., Raffi, I., Zachos, J.C., Wilkens, R.H.,
665 2017. Astronomical Calibration of the Ypresian Time Scale, Supplement to: Westerhold, T et
666 al. (2017): Astronomical calibration of the Ypresian timescale: implications for seafloor
667 spreading rates and the chaotic behavior of the solar system. Clim. Past 13, 1129-1152,
668 https://doi.org/10.5194/cp-13-1129-2017, PANGAEA.

669 Westerhold, T., Röhl, U., Donner, B., Zachos, J.C., 2018. Global Extent of Early Eocene
670 Hyperthermal Events: A New Pacific Benthic Foraminiferal Isotope Record From Shatsky Rise
671 (ODP Site 1209). Paleoceanogr. Paleoclimatol. 33, 626-642.
672 https://doi.org/10.1029/2017PA003306.

673 Zhao, N., Xu, X., Yu, H., Yao, J., Su, Q., Peng, S., 2011. The color reflectance of marine-
674 terrigenous deposits in LZ908 borehole in south coastal plain of Laizhou Bay. Acta Oceanol.
675 Sin. 30, 53–59. https://doi.org/10.1007/s13131-011-0133-4.

Supplementary materials

1 Materials and methods

Sampling and preparation of samples

In April 2016, the Integrated Ocean Discovery Program (IODP) and International Continental Scientific Drilling Program (ICDP) (Expedition 364) drilled a ~800 m-long core (Hole M0077A) in the Chicxulub crater (Gulick et al., 2017). Core was taken from 1334.69 to 505.70 meters below seafloor (mbsf) which captured the Cenozoic interval including the Cretaceous/Paleogene interval, the Paleocene Eocene Thermal Maximum (PETM) and the EECO. A previous biomarker study was conducted using core samples taken at a relatively lower resolution (62 samples between ~500 to 1300 mbsf) to investigate the post-impact recovery of life and paleoenvironmental conditions at the Chicxulub impact crater (Schaefer et al., 2020; Schaefer et al., 2022, accepted). Now, a total of 69 samples was taken from a ~12 m short interval between ~506.23-518.30 mbsf deposited at the end of the EECO (~48.3 to 48.8Ma) (Gulick et al., 2017; Morgan et al., 2016).

Each intact sample was surface-cleaned in an ultrasonic bath (10 min, three times), using a mixture of organic solvents dichloromethane (DCM) and methanol (MeOH) (9:1). All glassware including vials, beakers and pipettes were pre-cleaned and combusted at 500°C (8 hours) to avoid surface contamination.

Cyclostratigraphic analysis

Cyclostratigraphic investigations were carried out on colour data (L*- and a*-values) that were obtained from high-resolution line-scanning (Gulick et al., 2017). In order to obtain an evenly spaced dataset L*- and a*-data were linearly interpolated to an average sampling spacing of 2 cm. Thereafter, data were re-evaluated using the weighted-average rLOESS method.

Cyclostratigraphic analysis was performed in two steps. Firstly, the long record (~505.72 – 580 mbsf) was analysed to detect the stable 405 kyr eccentricity cycle (Berger and Loutre, 1994; Laskar et al., 2011; Laskar et al., 2004). Then the core interval from ~506 to 522 mbsf was analysed in detail, as the interval from ~505.72 to 520 mbsf was subjected to detailed geochemical investigations.

Cyclostratigraphic analysis was performed using the ACYCLE 2.3 tool for Matlab (Li et al., 2019). For spectral analysis the 2π multitaper method (MTM) was applied (Thomson, 1982) together with robust red noise models (Mann and Lees, 1996). The frequency ratio method was applied to the data set to test the data for the presence of astronomical frequencies (Boulila et al., 2008).

Evolutionary spectral analysis was done using Fast Fourier transform as implemented in the ACYCLE 2.3 tool for Matlab (Li et al., 2019). A sliding window size of 200 and step size of 2 was used. Evolutionary spectral analysis allows assessing the evolution spectral components along a section investigated. Statistically significant spectral peaks were filtered from the data series using Taner-Hilbert filtering (Taner, 2000).

Total organic carbon (TOC) content and Rock Eval analysis

Total organic carbon (TOC, wt. %) content was measured using a LECO carbon/sulfur analyzer. Rock-Eval pyrolysis was performed on each powered sample (~80 mg) using a Vinci Technologies Rock-Eval 6 standard analyzer with the IFP160000 standard to generate the thermal maturity parameters (S1, S2, Tmax and S3 peaks). The pyrolysis was programmed at an initial temperature of 300°C (held for 3 min) then heated to 650°C at a rate of 25°C/min.

Carbonate (TIC) content

Total carbon (TC) contents were directly measured on powered samples using a Vario CNS Elemental Analyzer III (Elementar®). Reproducibility and quality of the measurements were checked by running duplicate samples and standards every 10 sample. The total inorganic carbon (TIC) contents were subsequently calculated by subtracting TOC from TC. The carbonate content was calculated by multiplying the TIC by 8.33 (stoichiometry of $CaCO_3$).

$\delta^{13}C_{kerogen}$

$\delta^{13}C_{kerogen}$ was measured on decarbonated samples (1M HCl treatment for extracted sediments) using a Thermo Flash 2000 HT elemental analyser (EA) connected to a Delta V Advantage isotope ratio mass spectrometer (irMS) via a Conflo IV. Samples were weighed (~2 mg) in triplicate into tin cups (SerCon) and combusted to CO_2 in the nitrogen-carbon reactor (1020 °C). CO_2 passed through the Conflo IV interface into the irMS, which measured *m/z* 44, 45 and 46. $\delta^{13}C$ values were calculated by Thermo Isodat software and normalised to the international VPDB scale by multi-point normalisation using the standard reference materials NBS 19 (+1.95 ‰) and L-SVEC (-46.6 ‰) (Coplen et al., 2006). The standard reference material IAEA-600 was measured during the sequence to evaluate the accuracy of the normalization. The normalized $\delta^{13}C$ values of IAEA-600 from these measurements were within ± 0.1 ‰ of the reported value of -27.8 ‰ (Coplen et al., 2006).

$\delta^{34}S_{Pyrite}$

The sulfur isotope composition ($\delta^{34}S$) for total reduced inorganic sulfur (TRIS), considered to consist essentials as pyrite (FeS_2), is represented by $\delta^{34}S_{pyrite}$. The TRIS was extracted from powdered sediments *via* hot acidic chromium (II) chloride distillation, then the generated hydrogen sulfide was transported in a stream of nitrogen gas through a Zn acetate solution trap and precipitated quantitatively as ZnS (Fossing and Jørgensen, 1989). Sulfide concentrations

were measured spectrophotometrically by the methylene blue method (Cline, 1969). For isotope measurements, the trapped ZnS was transformed to Ag_2S with a 1 M $AgNO_3$ solution, washed and dried (*e.g.*, Koebsch et al., 2019). The sulfur isotopic composition was measured by combustion-isotope ratio monitoring mass spectrometry (C-irmMS) using a Thermo Scientific IsoLink elemental analyser coupled to a Thermo Finnigan MAT 253 mass spectrometer via a Thermo Scientific Conflo IV interface. Mass spectrometric results were calibrated to the V-CDT scale using IAEA isotope reference materials following Mann et al. (2009).

Biomarker analysis

Soxhlet extraction: The Soxhlet apparatus used for extraction were combusted at 500°C (8 hours) to remove any surface contamination. Before sample extraction, glass-fibre thimbles used for sample extractions were cleaned in Soxhlet apparatus using 9:1 DCM:MeOH until all traces of organic contaminants were removed. Each ground sample (between 6 ~ 7g) was weighed into the pre-cleaned glass-fibre thimble and was Soxhlet extracted with DCM and MeOH (9:1) (72 hours). At all times, parallel procedural blanks were taken for analyses. After extraction, activated copper turnings were added to extracts to remove potential elemental sulfur.

Column chromatography: Sediment extracts (~20 mg) were adsorbed onto activated silica gel and applied on the top of a pre-cleaned large column (20 cm) filled with 20 cm of silica gel. The saturate, aromatic and polar fractions were eluted from the column with the following solvents: *n*-hexane, 9:1 *n*-hexane:DCM, 1:1 DCM:MeOH. All the fractions were reduced to dryness by evaporation under a slow N_2 gas flow.

Gas chromatography – mass spectrometry (GC-MS): GC-MS was performed using an Agilent 5975B MSD interfaced to an Agilent 6890 gas chromatograph, which was fitted with a DB-1MS UI capillary column for saturated fractions and a DB-5MS UI capillary column for aromatic fractions (both columns J and W Scientific, 60 m, 0.25 mm i.d., 0.25 µm film thickness). Samples were dissolved in *n*-hexane and injected using an Agilent 7683B auto-sampler. The GC oven was ramped from 40 °C to 325 °C at a heating rate of 3 °C/min with initial and final hold times of 1 and 30 min, respectively. Helium was used as carrier gas at a constant flow of 1.1 mL/min. The MS was operated with a standardized ionization energy of 70 *eV*, a source temperature of 230 °C and an electron multiplier voltage of 1706 V, scanning a mass range of 50–550 Daltons (2.91 scans per second). Saturated and aromatic hydrocarbons were identified by comparison of mass spectra and by matching retention times with those of reference compounds reported previously (Grice et al., 2007; Grice et al., 1996). The mass spectrometer was operated in full scan mode to identify the compounds.

Gas chromatography – metastable reaction mode – mass spectrometry (GC-MRM-MS): Combined saturated and aromatic fractions with an internal standard added (D4-C_{27} ααα cholestane) were analysed by GC-QQQ (MRM)-MS at the Massachusetts Institute of Technology (MIT) for quantification, using an Agilent 7890B GC fitted with a DB-5MS UI capillary column (Agilent 122-5562 UI, 60 m, 0.25 mm i. d., 0.25 µm film thickness), connected to an Agilent 7010B triple quadrupole MS. Helium was used as carrier gas. The GC oven was ramped from 40°C to 325°C at a heating rate of 4°C/min with a holding time of 20.75 min at 325°C. The temperature of the QQQ was set to 150ºC. Compounds were identified by comparing retention time with reference compounds from GEOMARK standards. Specific compounds of interests were identified by comparison with reference standards, matching retention times and elution order (French et al., 2015). The following transitions were monitored: *m/z* 412 → 191 (C_{30} hopanes), *m/z* 372 → 217 (C_{27} steranes), *m/z* 386 → 217 (C_{28}

steranes), *m/z* 400 → 217 (C_{29} steranes), *m/z* 414 → 231 (C_{30} methylsterane), *m/z* 426 → 205 (C_{31} methylhopane), *m/z* 414 → 217 (24-*i*pc), *m/z* 414 → 217 (24-*n*pc), *m/z* 546 → 134 (paleorenieratane & isorenieratane & renieratane & renierapurpurane), *m/z* 552 → 134 (β-paleorenieratane & β-isorenieratane), *m/z* 554 → 134 (chlorobactane & okenane), *m/z* 558 → 123 (β-carotane), *m/z* 560 → 125 (γ-carotane), *m/z* 376.3 → 221 (D4-C_{27} ααα cholestane).

Gas chromatography – isotope ratio – mass spectrometry (GC-*ir*-MS): Compound-specific $\delta^{13}C$ measurements were performed using a Thermo Trace GC Ultra coupled to a Delta V Advantage irMS *via* a GC Isolink and Conflo IV. GC conditions were the same as described above for saturated compounds. Compounds eluted from the GC were combusted to CO_2 in the GC Isolink combustion furnace (CuO and NiO, held at 1020 °C). Peaks of CO_2 passed through the Conflo interface into the irMS, which measured *m/z* 44, 45 and 46. The $\delta^{13}C$ values were calculated from the measured masses by Thermo Isodat software and normalised to the VPDB scale by comparison with an in-house mixture of *n*-alkanes with known isotopic composition. All samples were analysed in triplicate.

2 Results

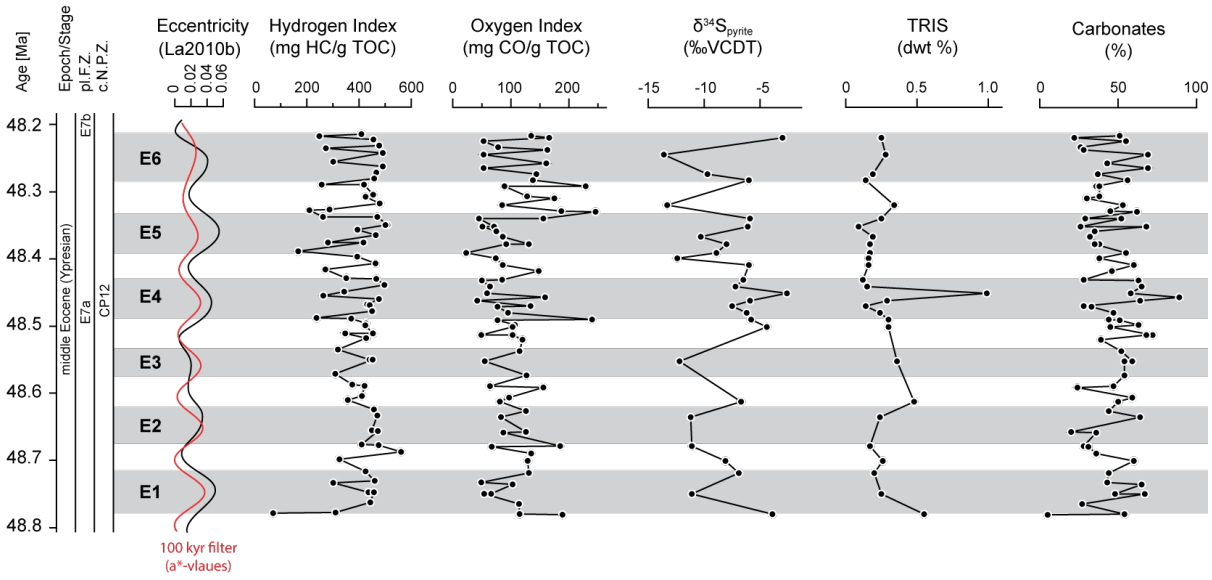

Figure S1 *HI and OI values, $\delta^{34}S_{pyrite}$ values (‰, VCDT), total reduced inorganic sulfur contents (dwt %), and carbonate contents (%) of analysed samples throughout the studied interval. Shaded areas represent intervals linked to anoxic conditions.* ***Shaded areas represent intervals linked to anoxic conditions.*** *E1 – E6 represent six short eccentricity cycles recorded throughout the interval of study. Eccentricity maxima (minima) measures how much the shape of Earth's orbit departs the most (the least) from a perfect circle.*

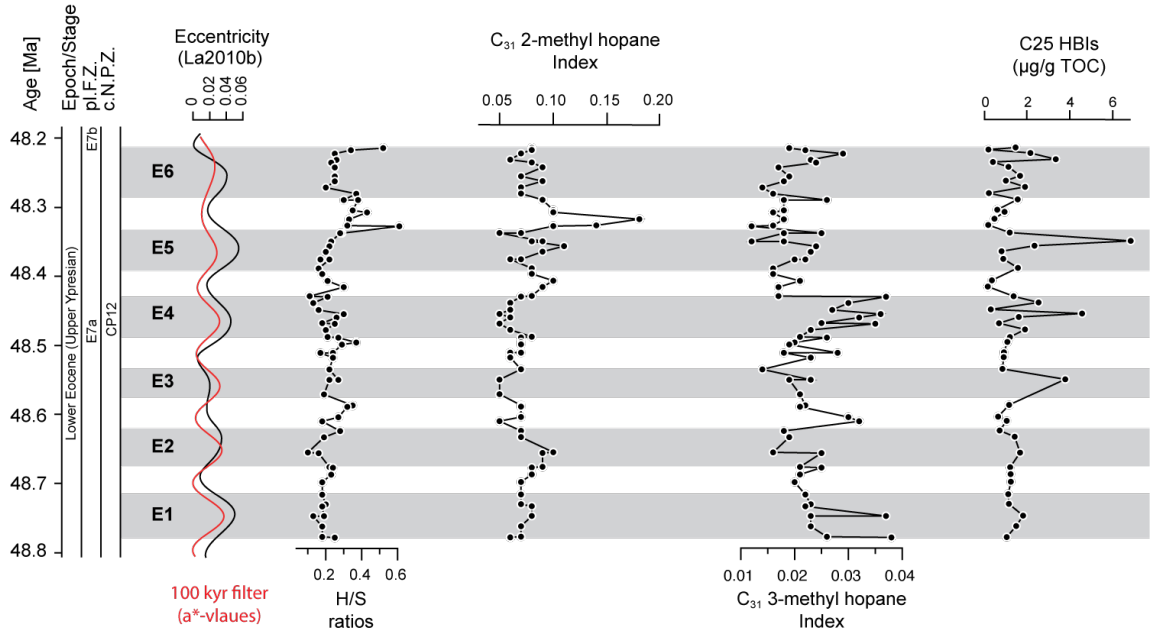

Figure S2 *Orbital frequency, biomarker data indicative of microbial community structures of analysed samples throughout the studied interval. E1 – E6 represent six short eccentricity cycles recorded throughout the interval of study. Eccentricity maxima (minima) measures how much the shape of Earth's orbit departs the most (the least) from a perfect circle. An interpretation of each data is indicated below: H/S ratios – bacterial input versus eukaryotic input; C_{31} 2-methylhopane Index – cyanobacteria; C_{31} 3-methylhopane Index – methanotrophs; C_{25} HBIs – diatoms. Shaded areas represent intervals linked to anoxic conditions.*

Table S1. *Distributions of maturity-sensitive biomarker parameters.*

Age (Ma)	C_{31} Hopane 22*S*/(22*S*+22*R*)	C_{30} Hopane βα/(βα+αβ)
48.215	0.19	0.11
48.218	0.22	0.10
48.223	0.31	0.14
48.232	0.24	0.11
48.236	0.24	0.11
48.243	0.37	0.13
48.256	0.22	0.11
48.263	0.29	0.12
48.272	0.30	0.12
48.281	0.19	0.11
48.290	0.22	0.11
48.290	0.19	0.12
48.305	0.20	0.12
48.308	0.18	0.12
48.318	0.24	0.10
48.327	0.25	0.11
48.328	0.16	0.12
48.338	0.27	0.11
48.338	0.22	0.11
48.350	0.28	0.11
48.350	0.30	0.13
48.357	0.30	0.13
48.365	0.27	0.10
48.376	0.24	0.10
48.376	0.24	0.11
48.389	0.25	0.12
48.397	0.28	0.10
48.407	0.23	0.11
48.416	0.21	0.10
48.429	0.28	0.10
48.430	0.29	0.14
48.439	0.29	0.18
48.449	0.26	0.15

48.455	0.27	0.14
48.460	0.31	0.16
48.468	0.25	0.11
48.469	0.30	0.14
48.478	0.25	0.11
48.488	0.23	0.11
48.489	0.26	0.15
48.496	0.23	0.12
48.499	0.21	0.12
48.511	0.32	0.14
48.511	0.24	0.10
48.518	0.29	0.12
48.535	0.25	0.09
48.550	0.27	0.13
48.550	0.23	0.11
48.571	0.23	0.10
48.587	0.26	0.14
48.589	0.20	0.11
48.604	0.29	0.14
48.610	0.27	0.14
48.624	0.23	0.11
48.633	0.27	0.10
48.655	0.23	0.10
48.656	0.29	0.13
48.676	0.22	0.09
48.677	0.30	0.12
48.687	0.25	0.11
48.698	0.26	0.12
48.716	0.24	0.10
48.730	0.26	0.14
48.733	0.26	0.11
48.747	0.30	0.14
48.747	0.25	0.11
48.762	0.26	0.10
48.777	0.23	0.11
48.778	0.18	0.11

Table S2. *Distributions of TOC contents, TRIS and* $\delta^{34}S_{pyrite}$ *for selected core samples.*

Age (Ma)	TOC	TRIS (*dwt*. %)	$\delta^{34}S_{pyrite}$ (‰ VCDT)
48.218	2.40	0.25	-3.0
48.243	2.22	0.28	-13.6
48.272	1.77	0.19	-9.7
48.281	0.81	0.14	-6.0
48.318	1.47	0.34	-13.3
48.338	1.53	0.25	-5.9
48.350	1.60	0.09	-6.1
48.365	1.36	0.19	-10.3
48.376	1.97	0.17	-8.0
48.389	2.08	0.17	-8.9
48.397	2.63	0.16	-12.4
48.407	1.40	0.16	-6.0
48.429	2.18	0.12	-6.5
48.439	2.12	0.15	-7.2
48.449	3.12	0.99	-2.6
48.460	2.78	0.29	-5.9
48.468	1.54	0.14	-7.5
48.478	1.40	0.24	-6.2
48.488	1.86	0.30	-5.8
48.499	1.37	0.30	-4.4
48.550	1.38	0.36	-12.2
48.610	3.86	0.48	-6.7
48.633	1.53	0.24	-11.2
48.676	0.89	0.17	-11.1
48.698	2.56	0.26	-8.1
48.716	1.11	0.20	-6.9
48.747	2.57	0.25	-11.1
48.777	2.20	0.55	-3.9

Table S3. *$\delta^{13}C$ values for Ph of selected samples and their standard deviations*

Age (Ma)	$\delta^{13}C$ of Ph (‰, VPDB)	Standard deviation
48.215	-32.0	(0.20)[3]
48.213	-31.9	(0.05)[3]
48.223	-31.4	(0.10)[3]
48.232	-32.3	(0.20)[3]
48.232	-32.0	(0.27)[3]
48.236	-31.5	(0.14)[3]
48.256	-31.5	(0.20)[3]
48.263	-30.7	(0.26)[3]
48.272	-31.7	(0.18)[3]
48.281	-32.0	(0.14)[3]
48.290	-31.5	(0.29)[3]
48.290	-31.7	(0.20)[3]
48.305	-32.1	(0.13)[3]
48.308	-33.8	(0.03)[3]
48.318	-31.9	(0.24)[3]
48.327	-31.7	(0.18)[3]
48.328	-31.0	(0.34)[3]
48.338	-32.0	(0.05)[3]
48.350	-30.6	(0.09)[3]
48.350	-31.1	(0.11)[3]
48.357	-31.7	(0.06)[3]
48.365	-32.7	(0.14)[3]
48.376	-31.8	(0.13)[3]
48.376	-31.7	(0.38)[3]
48.389	-31.9	(0.31)[3]
48.397	-31.1	(0.26)[3]
48.407	-32.0	(0.07)[3]
48.416	-32.9	(0.19)[3]
48.429	-32.3	(0.06)[3]
48.430	-32.1	(0.26)[3]
48.439	-32.2	(0.20)[3]
48.449	-32.2	(0.08)[3]

48.455	-31.6	$(0.02)^3$
48.460	-31.5	$(0.28)^3$
48.468	-32.0	$(0.34)^3$
48.469	-31.7	$(0.14)^3$
48.478	-32.2	$(0.05)^3$
48.488	-31.0	$(0.09)^3$
48.489	-30.0	$(0.95)^3$
48.496	-31.6	$(0.12)^3$
48.499	-32.3	$(0.07)^3$
48.511	-31.6	$(0.15)^3$
48.518	-31.7	$(0.22)^3$
48.535	-31.5	$(0.18)^3$
48.550	-30.5	$(0.22)^3$
48.550	-31.2	$(0.06)^3$
48.587	-31.8	$(0.13)^3$
48.589	-32.9	$(0.15)^3$
48.604	-31.5	$(0.14)^3$
48.610	-31.9	$(0.17)^3$
48.624	-31.5	$(0.33)^3$
48.633	-32.1	$(0.04)^3$
48.655	-30.0	$(0.31)^3$
48.656	-31.3	$(0.06)^3$
48.676	-29.1	$(0.04)^3$
48.677	-31.3	$(0.14)^3$
48.687	-31.6	$(0.34)^3$
48.698	-32.5	$(0.10)^3$
48.716	-32.0	$(0.06)^3$
48.730	-32.0	$(0.29)^3$
48.733	-32.6	$(0.02)^3$
48.747	-32.1	$(0.08)^3$
48.747	-30.5	$(0.32)^3$
48.762	-32.8	$(0.04)^3$
48.777	-32.3	$(0.15)^3$
48.778	-31.9	$(0.24)^3$

References:

Berger, A., Loutre, M.F., 1994. Precession, Eccentricity, Obliquity, Insolation and Paleoclimates, in Duplessy, J.C., Spyridakis, M.T. (Eds), Long-Term Climatic Variations. NATO ASI Series, 22. Springer, Berlin, Heidelberg. https://doi.org/10.1007/978-3-642-79066-9_5.

Boulila, S., Hinnov, L.A., Huret, E., Collin, P.-Y., Galbrun, B., Fortwengler, D., Marchand, D., Thierry, J., 2008. Astronomical calibration of the Early Oxfordian (Vocontian and Paris basins, France): Consequences of revising the Late Jurassic time scale. Earth Planet. Sci. Lett. 276, 40-51. https://doi.org/10.1016/j.epsl.2008.09.006.

Cline, J.D., 1969. SPECTROPHOTOMETRIC DETERMINATION OF HYDROGEN SULFIDE IN NATURAL WATERS1. Limnol. Oceanogr. 14, 454-458. https://doi.org/10.4319/lo.1969.14.3.0454.

Coplen, T.B., Brand, W.A., Gehre, M., Gröning, M., Meijer, H.A.J., Toman, B., Verkouteren, R. M., 2006. New Guidelines for $\delta^{13}C$ Measurements. Anal. Chem. 78, 2439-2441. https://doi.org/10.1021/ac052027c.

Fossing, H., Jørgensen, B.B., 1989. Measurement of bacterial sulfate reduction in sediments: evaluation of a single-step chromium reduction method. Biogeochemistry 8, 205–222. https://doi.org/10.1007/BF00002889.

French, K.L., Hallmann, C., Hope, J.M., Schoon, P.L., Zumberge, J.A., Hoshino, Y., Peters, C.A., George, S.C., Love, G.D., Brocks, J.J., Buick, R., Summons, R.E., 2015. Reappraisal of hydrocarbon biomarkers in Archean rocks. Proc. Natl. Acad. Sci. 112, 5915-5920. https://doi.org/10.1073/pnas.1419563112.

Grice, K., Nabbefeld, B., Maslen, E., 2007. Source and significance of selected polycyclic aromatic hydrocarbons in sediments (Hovea-3 well, Perth Basin, Western Australia) spanning the Permian–Triassic boundary. Org. Geochem. 38, 1795-1803. https://doi.org/10.1016/j.orggeochem.2007.07.001.

Grice, K., Schaeffer, P., Schwark, L., and Maxwell, J. R., 1996. Molecular indicators of palaeoenvironmental conditions in an immature Permian shale (Kupferschiefer, Lower Rhine Basin, north-west Germany) from free and S-bound lipids. Org. Geochem. 25, 131-147. https://doi.org/10.1016/S0146-6380(96)00130-1.

Gulick, S.P.S., Morgan, J.V., Mellett, C.L., Green, S.L., Bralower, T., Chenot, E., Christeson, G., Claeys, P., Cockell, C., Coolen, M.J.L., Ferrière, L., Gebhardt, C., Goto, K., Jones, H., Kring, D., Lofi, J., Lowery, C., Ocampo-Torres, R., Perez-Cruz, L., Pickersgill, A.E., 2017. Chicxulub: Drilling the K-Pg Impact Crater. Proceedings of the International Ocean Discovery Program, 364: College Station, TX (International Ocean Discovery Program). https://doi.org/10.14379/iodp.proc.364.2017.

Koebsch, F., Winkel, M., Liebner, S., Liu, B., Westphal, J., Schmiedinger, I., Spitzy, A., Gehre, M., Jurasinski, G., Köhler, S., Unger, V.R., Koch, M., Sachs, T., Böttcher, M.E., 2019. Sulfate deprivation triggers high methane production in a disturbed and rewetted coastal peatland. Biogeosciences, 16, 1937-1953. https://doi.org/10.5194/bg-16-1937-2019.

Laskar, J., Fienga, A., Gastineau, M., Manche, H., 2011. La2010: a new orbital solution for the long-term motion of the Earth⋆. Astron. Astrophys. 532, A89. https://doi.org/10.1051/0004-6361/201116836.

Laskar, J., Robutel, P., Joutel, F., Gastineau, M., Correia, A.C.M., Levrard, B., 2004. A long-term numerical solution for the insolation quantities of the Earth. Astron. Astrophys. 428, 261-285. https://doi.org/10.1051/0004-6361:20041335.

Li, M., Hinnov, L., Kump, L., 2019. Acycle: Time-series analysis software for paleoclimate research and education. Comput. Geosci. 127, 12-22. https://doi.org/10.1016/j.cageo.2019.02.011.

Mann, J., Vocke, R., Kelly, W., 2009. Revised δ 34 S reference values for IAEA sulfur isotope reference materials S-2 and S-3. Rapid Commun. Mass Spectrom. 23, 1116-1124. https://doi.org/10.1002/rcm.3977.

Mann, M.E., Lees, J.M., 1996. Robust estimation of background noise and signal detection in climatic time series. Clim. Change 33, 409-445. https://doi.org/10.1007/BF00142586.

Morgan, J.V., Gulick, S.P.S., Bralower, T., Chenot, E., Christeson, G., Claeys, P., Cockell, C., Collins, G.S., Coolen, M.J.L., Ferrière, L., Gebhardt, C., Goto, K., Jones, H., Kring, D.A., Le Ber, E., Lofi, J., Long, X., Lowery, C., Mellett, C., Ocampo-Torres, R., Osinski, G. R., Perez-Cruz, L., Pickersgill, A., Poelchau, M., Rae, A., Rasmussen, C., Rebolledo-Vieyra, M., Riller, U., Sato, H., Schmitt, D. R., Smit, J., Tikoo, S., Tomioka, N., Urrutia-Fucugauchi, J., Whalen, M., Wittmann, A., Yamaguchi, K.E., Zylberman, W., 2016. The formation of peak rings in large impact craters. Science, 354, 878-882. https://doi.org/10.1126/science.aah6561.

Schaefer, B., Grice, K., Coolen, M.J.L., Summons, R.E., Cui, X., Bauersachs, T., Schwark, L., Böttcher, M.E., Bralower, T.J., Lyons, S.L., Freeman, K.H., Cockell, C.S., Gulick, S.P.S., Morgan, J.V., Whalen, M.T., Lowery, C.M., Vajda, V., 2020. Microbial life in the nascent Chicxulub crater. Geology, 48, 328-332. https://doi.org/10.1130/G46799.1.

Schaefer, B., Schwark, L., Böttcher, M. E., Smith, V., Coolen, M. J. L., and Grice, K., 2021, Paleoenvironmental evolution during the Early Eocene Climatic Optimum in the Chicxulub impact crater. Earth and Planetary Science Letters, accepted.

Taner, M.T., 2000. Attributes Revisited, Technical Report. Rock Solid Images, Inc. http://www.rocksolidimages.com/pdf/attrib_revisited.htm.

Thomson, D. J., 1982. Spectrum estimation and harmonic analysis. Proc. IEEE Inst. Electr. Electron Eng. 70, 1055-1096. https://doi.org/10.1109/PROC.1982.12433.